The Pennsylvania State University

The Graduate School

Department of Physics

WEAK FERROMAGNETISM IN DILUTE MANGANESE-NICKEL ALLOYS

A Dissertation in

Physics

by

Kenneth Podolak

Submitted in Partial Fulfillment
of the Requirements
for the Degree of

Doctor of Philosophy

August 2008

The dissertation of Kenneth Podolak was reviewed and approved* by the following:

Roy F. Willis
Professor of Physics
Dissertation Advisor
Chair of Committee

Peter Schiffer
Professor of Physics

Renee Diehl
Professor of Physics

Darrell Schlom
Professor of Materials Science & Engineering

Dr. Jayanth Banavar
Professor of Physics
Head of the Department of Physics

*Signatures are on file in the Graduate School

ABSTRACT

Nickel manganese alloys are interesting due to their novel magnetic behavior. At low concentrations of manganese, the alloys show increased ferromagnetism at room temperature. Increasing the concentration to 25% manganese in nickel results in a frozen spin glass with reduced ferromagnetism. The transition from one state to the other is of fundamental interest. Furthermore, magnetic alloy thin films have widespread application in magnetic memory devices.

By diffusing manganese into a nickel single-crystal substrate, spin scattering effects in the sp bands were explored. The behavior was compared with that of chromium and iron-doped nickel alloys. The results show that the behavior in manganese-doped nickel to be different in both the change in the exchange field and the spin transport properties.

I have built a vapor deposition system to investigate nickel manganese alloys characterized with surface science techniques, namely reflection high energy electron spectroscopy (RHEED), low energy electron diffraction (LEED), and scanning electron microscopy (SEM).

Samples were grown on Si(100) with buffer layers of copper sandwiching the nickel manganese alloy. Magnetic hysteresis loops and magnetic circular dichroism (MCD) signatures show a transition in the magnetism at 15% manganese in nickel when measured at 100K. This transition is a sign of this alloy entering a re-entrant spin glass (RSG) magnetic phase. Thermal hystersis measurements confirm that the spin glass freezing temperature for a 10% manganese in nickel sample is around 100K.

The measurements endorse the unusual precursor spin-glass behavior of dilute ferromagnetic alloys of manganese in nickel. With increasing doping, the nickel first shows increased ferromagnetism followed by spin disordering and the formation of a spin glass.

TABLE OF CONTENTS

LIST OF FIGURES

Chapter 1

Chapter 2

Chapter 3

Chapter 4

Chapter 5

LIST OF TABLES

ACKNOWLEDGEMENTS

Many thanks goes to those who have helped me reach this ultimate goal. I couldn't have achieved my goals without the direction of my advisor, *Dr. Roy Willis.* He is always there to give advice and to help compromise his goals with my passions in research. It is through him I learned how to do research and "use my hands" for the first time. I also would like to thank my research group members and past postdocs: *Hyosig Won, Yu Liu, Tim Bramfeld, Bangzhi Liu, Ted Kreutz, and Michael Birke*. Together we all bonded and learned from each other as the research program grew. *Hyosig Won* and *Yu Liu* I emphasize due to their extra efforts in times of great need.

I would like also to thank my wonderful family that gave me the basis to be where I am today. My mom, *Nancy*; dad, *Ken*; and brother, *Darren* all gave me the tools necessary to prosper. Lastly, I would like to thank my wife, *Marcia Capurso*. She is a source of inspiration and is always there for me when I need it. I am so proud of our relationship and look forward to spending every day together.

Chapter 1

Introduction……

1.1. Historical Precedents

At an early age in one's youth, many have discovered the unique forces of magnetism by feeling the attraction and repelling of two magnets. One of the most interesting aspects is that the force occurs at distances without any media between them. Feeling that force of repelling two opposite sides of a magnet strikes interest as to what makes magnetism occur.

Magnetism has had an illustrious past full of discovery. Magnetism was first used by the Chinese somewhere between 18^{th} and 12^{th} century B.C. when they discovered naturally occurring magnets known today as lodestones [1]. These lodestones would be used to map out directions, similar to the modern day compass. Around the same time, Greeks made similar discoveries in magnetism. In the 6^{th} century B.C. the Greek philosopher, Thales of Miletus, considered if these magnetic stones had a soul of their own [2]. Through the 1700's and 1800's many great scientists helped unify electricity and magnetism, furthering the applications of magnetism. Yet the secrets as to what causes the magnetism inside a material remained a mystery until the advent of quantum mechanics.

The modern field of magnetism began with Pierre Curie in 1895 with his study of magnetic temperature dependence of several substances [3]. From this an empirical relation known as Curie's law helped classify magnetic substances into different categories: paramagnetic and diamagnetic (and later on ferromagnetic). Diamagnetic and paramagnetic both need an external field to become magnetized. A ferromagnet such as iron retains magnetic properties with the absence of an applied field. Below a critical temperature, called the Curie temperature (T_C), spontaneous magnetic order occurs.

The first to discuss the origin of the atomic moment in iron was Pierre-Ernest Weiss in 1919. He described an effective interaction that electrons mimic in a magnetic field. This is called the 'exchange interaction' that appears in quantum mechanics. Weiss was also the first to discuss magnetic domains that cause the moments in some regions of iron to add up to a total moment of zero. In other regions, the domains of moments may exist, but align in a preferential direction [4].

In 1922, Stern-Gerlach set up an experiment to determine whether particles have an intrinsic angular momentum, known as spin angular momentum. The magnetic moment was already understood to have orbital contributions, but it was not known if the electron has its own contribution. Silver atoms were passed through an inhomogeneous magnetic field. If there was no spin angular momentum component, their distribution on a screen should be truly random. Instead, the atoms were deflected either up or down by a quantized

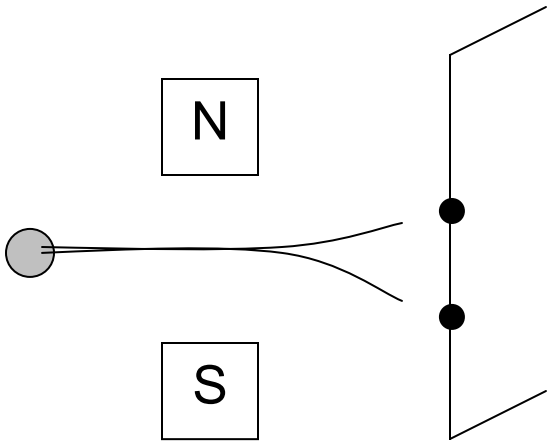

Figure 1: Schematic showing how the Stern-Gerlach experiment works. The beam of atoms (or electrons, shown on the left) is deflected by an inhomogeneous magnetic field. The results of two possible locations are predicted by quantum mechanics.

amount, as shown in figure 1. This proved that there are only quantized amounts of angular momentum, helping verify quantum mechanical predictions [5].

Slater and Pauling in the 1930's used neutron scattering data to plot how the magnetism is changing over a range of alloys and concentrations as shown in figure 2 [6]. This is a volcano style plot that empties the d shell going from right to left. On the right hand side are ferromagnetic metals such as nickel, cobalt, and iron. On the left side is a pure anti-ferromagnet, chromium. This plot shows that as the d shell is emptied, the magnetization increases, then decreases. Different trends also exist for different alloys of nickel. Nickel alloyed with increasing concentrations of cobalt (a ferromagnet) increases the magnetization as expected. Increasing concentrations of chromium (an antiferromagnet), decreases the magnetization as expected. Manganese doping of nickel at first increases the magnetization then decreases the magnetization for larger concentrations of manganese in nickel. This is also shown in figure 2.

1.2. Theoretical Basis

Two ways a sample can be magnetized is either it is naturally magnetic or it becomes magnetic with an applied field. If a field is applied to become magnetic, it is referred to as paramagnetic. Once the field is removed, the sample is no longer paramagnetic. Magnetic exchange energy is defined in the equation:

$$H_J = \sum J_{ij} (\vec{S}_i \bullet \vec{S}_j) \qquad (1)$$

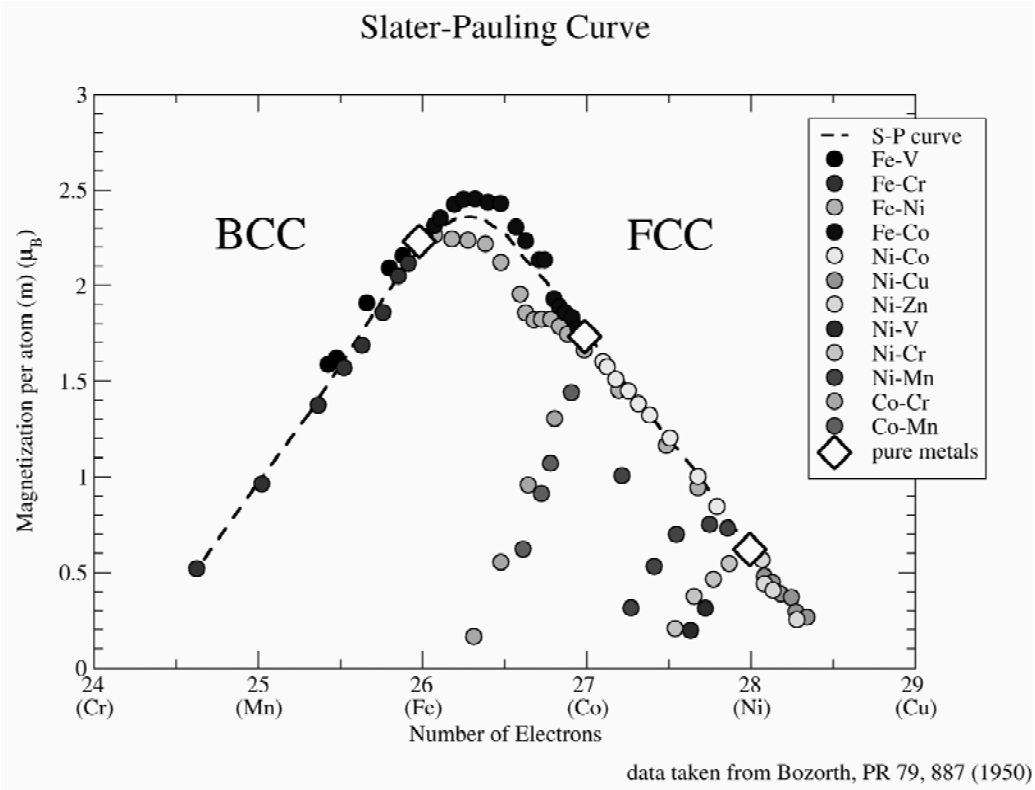

Figure 2: Slater-Pauling curve of magnetism measured from neutron-scattering data. This volcano plot shows the transition from ferromagnetism to antiferromagnetism, but questions remain as to why this transition occurs.

where S is the magnetic spin vector and J is the magnetic exchange strength. If the material is naturally magnetic and the interaction between the atoms is positive, namely a positive J in the Heisenberg Hamiltonian (equation 1), the material is labeled as a ferromagnetic. If however J is negative, antiferromagnetic order occurs where moments are aligned antiparallel. Since there is no net magnetic moment for antiferromagnets, they are not as easy to study as ferromagnets. In the case for spin glasses, a distribution of coupling constants cancel each other out so that $\Sigma J_{ij} = 0$.

A small applied magnetic field is one method to measure the magnetization of the sample. The external magnetic field energy is known as the Zeeman energy and changes the Hamiltonian to:

$$H_B = \sum J_{ij}(\vec{S}_i \bullet \vec{S}_j) - \mu_B \vec{B} \bullet \vec{H} \qquad (2)$$

where H is the applied magnetic field and B is the total magnetization of the spin configuration which can be written as:

$$\vec{B} = \sum \vec{S}_i \qquad (3)$$

All the information on a system can be contained in the partition function Z, which is an important thermodynamic quantity. All macroscopic theromodynamic quantities can be calculated from Z, e.g. the free energy of the system (F):

$$F = U - TS \tag{4}$$

where U is the internal energy of the system and S is the entropy of the system. The free energy is related to the partition function Z through:

$$F(T,B) = -k_B T \ln Z(T,B) \tag{5}$$

The partition function can be related to the Hamiltonian by:

$$Z(T,B) = \sum_{states} \exp(-H / k_B T) \tag{6}$$

The overall magnetization of a system <M> is defined for a particular magnetic spin state. This can be written as:

$$< M >= \frac{-1}{\mu_o V} \frac{\partial^2 F}{\partial H^2} \tag{7}$$

where V is the volume of the system. The magnetization reflects the change in energy associated with the presence of an applied magnetic field. A perturbation to the system is known as the susceptibility χ. This yields:

$$\chi = \frac{\partial < M >}{\partial H} = \frac{-1}{\mu_o V} \frac{\partial^2 F}{\partial H^2} \tag{8}$$

In order to investigate magnetic states of a system, one can use a small dc magnetic field as well as an oscillatory ac-field as we will see later in this thesis. This theoretical understanding is based on Huang and more can be found in this book [7].

1.3. Exchange Interaction

Magnetic moments in ferromagnetic or antiferromagnetic materials couple to one another to form magnetically ordered states. This coupling is known as an exchange interaction. The coupling in between the spins in metals can be due to direct exchange which is nearby and indirect exchange which is farther distances than distances between neighboring electrons.

Direct exchange occurs when magnetic moments are so close that their wavefunctions overlap. This coupling is strong, but decreases rapidly as you get farther from the moments. This exchange can have a positive or negative coupling constant J depending on a balance between neighboring moments. A magnitude of the direct exchange as a function of interatomic distance has been plotted, known as the Bethe-Slater curve, figure 3. We note that manganese has a negative coupling constant, while nickel has a positive coupling constant. It is this interaction between the nickel's positive coupling and manganese negative coupling that provides interest as to when antiferromagnetic behavior begins to dominate.

Indirect exchange occurs between non-neighboring electrons, therefore indirect exchange is dominant in conducting metals. This exchange is referred to

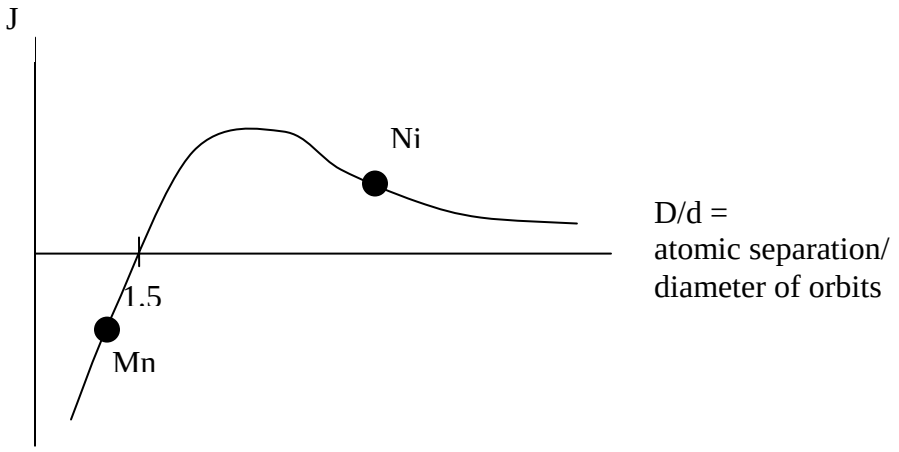

Figure 3: The Slater-Bethe curve showing the magnitude and sign of the exchange integral as a function of D/d or magnetic material. We note nickel with a positive J and Mn with a negative J.

as RKKY named after Ruderman, Kittel, Kasuya, and Yoshida [8]. The "J" coefficient in indirect exchange oscillates and decays between positive and negative J values as you get farther from the magnetic moment. Therefore the magnetic coupling may be ferromagnetic or antiferromagnetic based on the separation distance.

1.4. Aim of Research

In order to better understand antiferromagnetism, experiments can be done starting with permanent magnets such as nickel to see how the ferromagnetism changes with the addition of antiferromagnetic moments.

Nickel is an itinerant sea of magnetic spins (on average 0.6 per Ni atom). The manganese atoms effectively substitute for nickel atoms with a permanent and larger magnetic moment, roughly six times larger. It is believed that the interaction between nickel and manganese is generally ferromagnetic, while the interaction between manganese atoms is antiferromagnetic. The Slater-Pauling curve for nickel manganese alloys first increases in magnetism, followed by a decrease in magnetism, over a range of concentration, $0 \leq x \leq 25\%$. This behavior, however, is not reflected in T_C, which does not initially increase but decreases continually with Mn-dopant concentration [9]. The variation of the mean moment (saturation magnetization per atom) and T_C with Mn-dopant concentration is reproduced in figure 4.

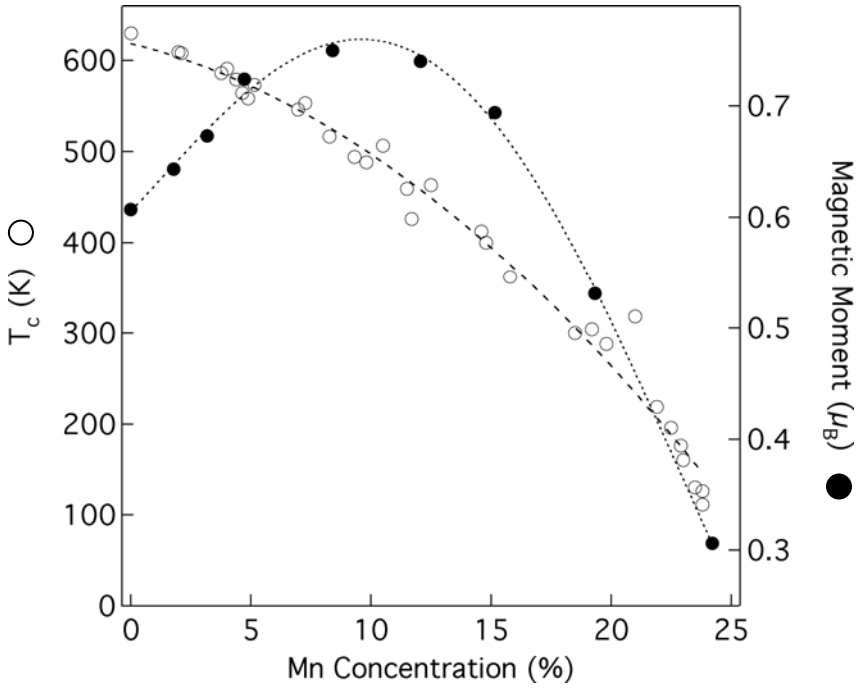

Figure 4: Data for the mean moment μ and Curie temperature T_C change with Mn-doping concentration of ferromagnetic Ni host.

If we are to better understand how magnetism changes based on the interaction between nickel and manganese atoms, this alloy has those necessary properties.

In this thesis, we investigate manganese-doping of nickel, which is of interest in magnetic sensors and recording heads [10]. The magnetic hard drives application of the giant magnetoresistance and read heads using spin valves [11] need a soft ferromagnet that is will provide the stable switching required in industry. Also, $Ni_{50}Mn_{50}$ has been of considerable interest as a pinning layer in exchanged bias systems. Much research has been done by sputtering NiMn with ferromagnetic layers [12] [13].

1.5. Outline of Thesis

This work focuses on the magnetic properties of nickel manganese alloys. In chapter two, the experimental approach is introduced including sample preparation and theoretical background to understand the tools and underlying principals required. In chapter three, the sp-bands of nickel manganese are looked at as they cross the Fermi energy. These results show new insights as to how the magnetism is handled at a band structure level. Chapter four discusses how these alloys transition from ferromagnetism into a spin glass by performing hysteresis loop measurements, both as a function of temperature and concentration, as well as magnetic circular dichroism measurements to look at the local magnetization results. Measurements are also done to distinguish local (from X-ray Magnetic Circular Dichroism) and non-local (from magnetic hysteresis loops) magnetic behavior. Chapter five is a case study of 10%

manganese in nickel, showing how the magnetism changes by looking at AC susceptibility and field cooling measurements. Lastly, conclusions and future directions are wrapped up in chapter six.

Chapter 2

Experimental Approach……..……

2.1. Sample Preparation

2.1.1. Sample Cleaning

In order to grow an ordered structure, sample substrates need to be cleaned free of contaminants such as oxygen, nitrogen, and carbon. The silicon <100> substrates were cleaned first by a series of chemical solvents using an ultrasonic bath. After each step, a rinse in deionized water was used. The order and time for each solvent was: acetone for five minutes, isopropanol for ten minutes, and methanol for five minutes. Lastly, the silicon is heated to 500 degrees Celcius in vacuum of roughly 10^{-9} Torr.

When a copper or nickel substrate was used, a different cleaning procedure was invoked as followed by Musket [14]. Hand polishing of the single crystal was done, starting with the highest grit polishing paper and working down to smaller grit. Each step the sample is rotated 90 degrees so that when the previous scratches disappear, we know we have polished enough with that sand paper. Pastes with beads are also used for fine polishing. Once in vacuum, the

sample goes through several cycles of annealing and argon bombardment. Argon bombardment involves blasting argon molecules onto the surface of the substrate so that it knocks away atoms. This creates some roughness in the sample which is smoothed out by heating. The pressure must be monitored when releasing argon so that contaminants will not pollute the sample during bombardment. Most argon bombardment experiments were performed at 1×10^{-6} Torr or less.

2.1.2. Molecular Beam Epitaxy

Good sample preparation is important to provide a good template for growing any material. The samples measured in chapters 4 and 5 were created using homemade vapor deposition evaporators. These evaporators were home-built on a 2 ¾ inch flange with electrical feedthroughs, as shown in figure 4. Pieces in the evaporator are made primarily of tantalum except for the ceramics for isolation. Tantalum is preferred due to its high melting point (1800 degrees Celsius) and ease of machining. The boats are made of tantalum for materials such as copper and manganese and tungsten for nickel. Tantalum is not used for nickel because nickel alloys with tantalum and eventually destroys the tantalum boat.

A tantalum filament is used between two posts and directly heated in ultra-high vacuum. This provides electron bombardment heating in no preferential direction. A high voltage is applied to a dish nearby the filament. This creates an electric field between the filament and the high voltage dish. Electrons now follow

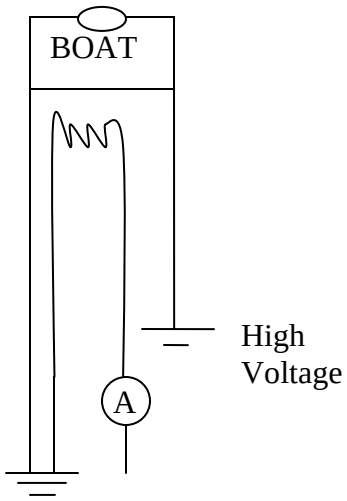

Figure 5: Evaporator complete with boat and filament underneath. Material to be evaporated is deposited into the boat.

the field and heat the dish. As temperature increases, the pressure increases. Since we would like to have the lowest pressure possible to ensure uniform growth, cooling fans are used on the outside of chamber.

2.1.3. Quartz Crystal Monitor (QCM)

A quartz crystal microbalance (QCM) is used to monitor the rate of metal ions and some neutral atoms coming from the evaporator (and a negligible amount from the surroundings). A quartz crystal operates by the Piezoelectric effect, namely that an electric potential is created by the quartz crystal by a stress. An alternating current is applied to a quartz crystal, causing a resonant frequency in the megahertz range. The frequency of oscillation of the crystal depends on the thickness of the crystal. As material is deposited, the crystal will decrease in frequency. The difference in frequency is used to measure the thickness deposited in a given sample time. The sensitivity is as small as 0.01 nm a minute.

It is important to keep the quartz crystal at a constant temperature. Water cooling is applied so that as the hot atoms strike the surface of the quartz crystal, they will not evaporate away, so water cooling is important to insure a proper reading. When reading measurements during an evaporation, it is important to make certain that the flux has reached a steady state so that the desired materials are deposited and are uniform in composition.

2.1.4. Evaporation Curve

Each evaporator and material produces a unique evaporation curve. An example of one such curve is given in figure 5. This curve was taken by evaporating copper in a tantalum boat roughly 1 meter away from the quartz crystal. The measurements were done at a constant filament current and the power applied to the boat was varied by changing the high voltage. As the voltage increases, the power increases due to the extra electrons that are attracted due to the higher potential. At first, no emission is detected. The first measurement of evaporation can occur suddenly, so care must be taken when the values are close to expected results.

Each metal has specific temperatures to which it will start to evaporate and melt. Some of the common materials used in these experiments are shown in table 1. Evaporation temperatures vary versus pressure, so all temperatures shown are given at 1×10^{-8} Torr which is a common pressure used during deposition for my experiments. Tantalum and tungsten have a much higher temperatures for melting and evaporating than that of the metals we wish to evaporate. It's important to keep the integrity of our evaporator while heating it up.

Evaporation curves are specific to each experiment. These rates can be higher or lower depending on the vacuum pressure, distance between the evaporation and detection, and the experimental geometry. Before depositing, the evaporator needs to be degassed or heated up to half the evaporation

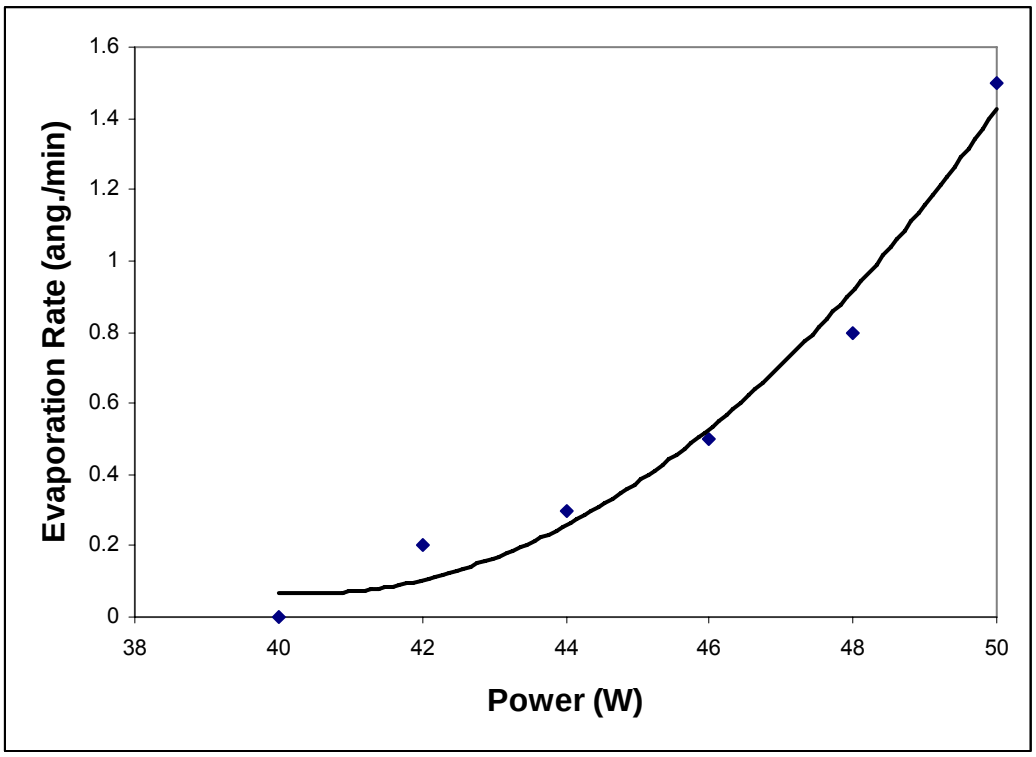

Figure 6: Evaporation rate vs. power applied to a tantalum boat with copper. Deposition rates are taken after a long time to make certain it is a stable reading. The solid curve is a guide to the eye, however the take off is quick. Results may vary based on evaporator and material.

Material	Evaporation Temperature (^{o}C)	Melting Temperature (^{o}C)
Cu	800	1083
Mn	900	1245
Ni	1100	1453
Ta	2200	2996
W	2500	3410

Table 1: Evaporation and melting temperatures for common metals used during my experiments. Note that the evaporation temperatures are all at 10^{-8} Torr and will vary based on pressure.

temperature of materials used to build the evaporator so that contaminants are expelled.

Keeping the vacuum pressure as low as possible is important during the sample preparation. One reason is to allow for the longest mean free path so that the material desired to be deposited has not strayed from its path. Another reason is that the surface of the substrate can be contaminated by stray particles if the pressure is not kept low enough. I make sure the pressure does not exceed 1×10^{-7} Torr during any degassing phase. During this deposition the pressure is approximately 1×10^{-8} Torr.

After the film is grown, we do not anneal the film so that the composition is metastable. Annealing a film can result in removal of defects or reordering of the films surface/interface. Also annealing can separate the films components into domains, creating a non-randomized lattice. In order to examine an alloys randomized magnetic state, the sample is held at room temperature.

2.1.5. Preparation Chamber

For the deposition to occur, I designed my own preparation chamber as shown in figure 7. This chamber is composed of two parts: the main chamber and load lock. Each section has its own turbo pump which is backed by a roughing pump. The pressure is constantly monitored using a pirani gauge at pressures greater than 10^{-3} Torr and an ion gauge for pressures less than 10^{-3} Torr.

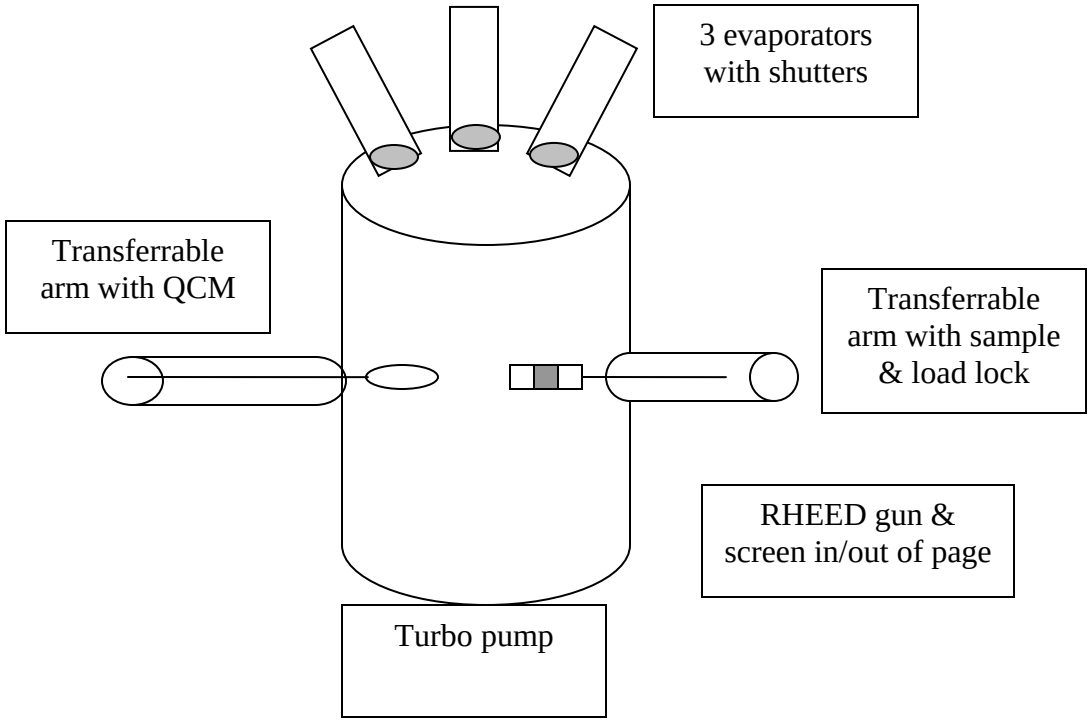

Figure 7: Preparation chamber schematic showing the sample transfer arm that is capable of heating, a QCM arm capable of moving into position, 3 homemade evaporators, turbo pumps and RHEED gun/screen.

The sample holder consists of a long rod and mounting clips separated by ceramics. Wires are connected to the mounting clips to allow for direct heating of the silicon sample. A viewing window is available to see the sample change color when heating.

The evaporators are installed at the top of the main chamber. Shutters are installed underneath evaporators where co-evaporation is expected to take place. Once one of the evaporators is cooking and evaporating at a stable rate, that evaporator is shuttered off from the QCM. The second evaporator is then turned on and its rate is stabilized. Constant checking of each evaporator is important to ensure proper concentrations. The concentrations can later be verified accurately using core level atomic spectroscopy either using tools in the laboratory (QCM) or x-ray photomission spectroscopy at a synchrotron facility (discussed in 2.6).

2.1.6. Growth

When depositing a thin film, growth onto the substrate can occur in many different ways. See figure 8 for a sketch of the three growth modes. The key in differentiating how a film is grown is the interactions between the surface and adatoms or evaporant material. In Volmer-Weber (VW) growth, the interactions between adatoms evaporated are stronger than those on the surface, which leads to clusters or islands on the surface. Metals grown on glasses or oxides often exhibit this growth [15].

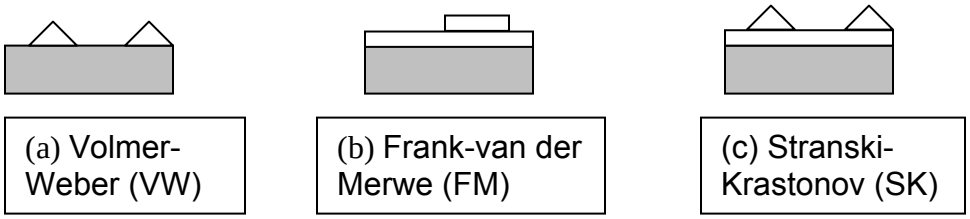

Figure 8: Three growth modes showing (a) island formation for VW growth, (b) layer-by-layer for FM growth, and (c) a combination of the first two for SK growth.

In Frank-van der Merwe (FM) growth, the adatoms evaporated form smooth layer-by-layer growth by bonding to the surface. FM growth occurs for well matched lattices, producing little strain. Lastly, Stranski-Krastonov (SK) growth occurs when growth starts out as layers and eventually goes into island growth. Bauer has reviewed these growth modes and classified them appropriately [16]. Not every alloy created is easy to predict which growth mode will happen, however if the lattice strain is small and the deposition rate is slow, layer-by-layer FM growth will more likely occur, at least for the films prepared in this work grown on copper (100).

2.1.7. Electrochemical Deposition

Another method to grow magnetic materials is electroplating or electrochemical deposition. This method is desirable due to its quick, yet cost-effective technique for preparing film coatings, with a new application into magnetic films [17] [18]. Magnetic alloy films are deposited onto n-silicon(100) substrates. A standard three electrode electrochemical cell was used, as seen in figure 9. An external circuit, primarily an op amp, maintained the silicon cathode at a constant electrochemical potential and supplied current through a metal anode. Alloy deposition was achieved by with an electrolyte solution containing ions of both metals. Teflon tape defines the deposition area on the silicon wafer, preventing deposit on the back and edges. Magnetic hysteresis was studied with a SQUID magnetometer, see section 2.3 for further details.

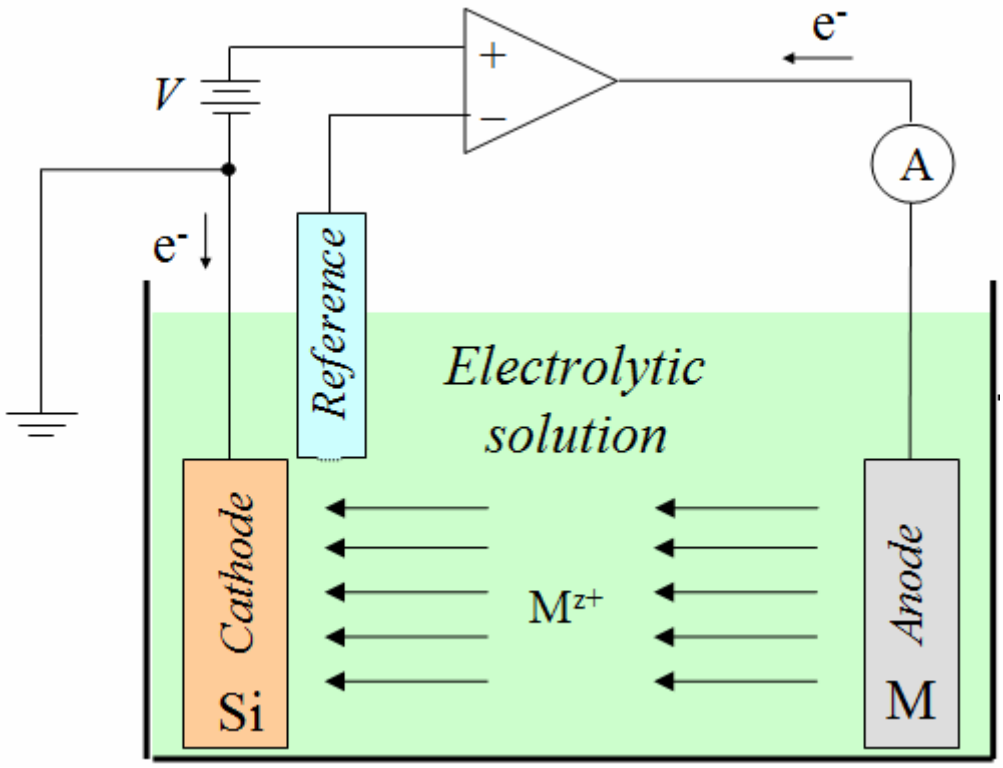

Figure 9: Electrochemical cell schematic. The op-amp receives negative feedback through a porous frit in the reference electrode. The cathode is maintained at a potential –V. A resistor is used as feedback into the op. amp. [19]

An equilibrium electric potential characterizes the reaction. An applied potential moves the reaction away from equilibrium, resulting in a net current and oxidation or reduction at an electrode. The energy bands bend at the surface of a silicon cathode in an electrolyte solution. There exists a space charge near thesurface, both in the silicon and solution. Conduction band electrons are accepted by ions in solution [20] [21]. For an electrode of metal M in contact with ions of the same species in aqueous solution, there is a reaction where the metal dissociates into electrons collected and metal ions in the bath. The equation for this is written as:

$$\mathrm{M} \leftrightarrow \mathrm{M}^{z+} + ze^{-} \tag{9}$$

The thickness of each sample can be estimated by theoretical formulas:

$$d = \frac{a^3 Q}{zeAn_{cell}} \tag{10}$$

$$Q = \int i \, \mathrm{d}t \tag{11}$$

where a = unit cell length, z = ionization state, A = deposition area, and n_{cell} = number of atoms per unit cell.

During deposition, the current or current density (current/area) can be measured versus time to get a deposition rate curve as seen in figure 10. The

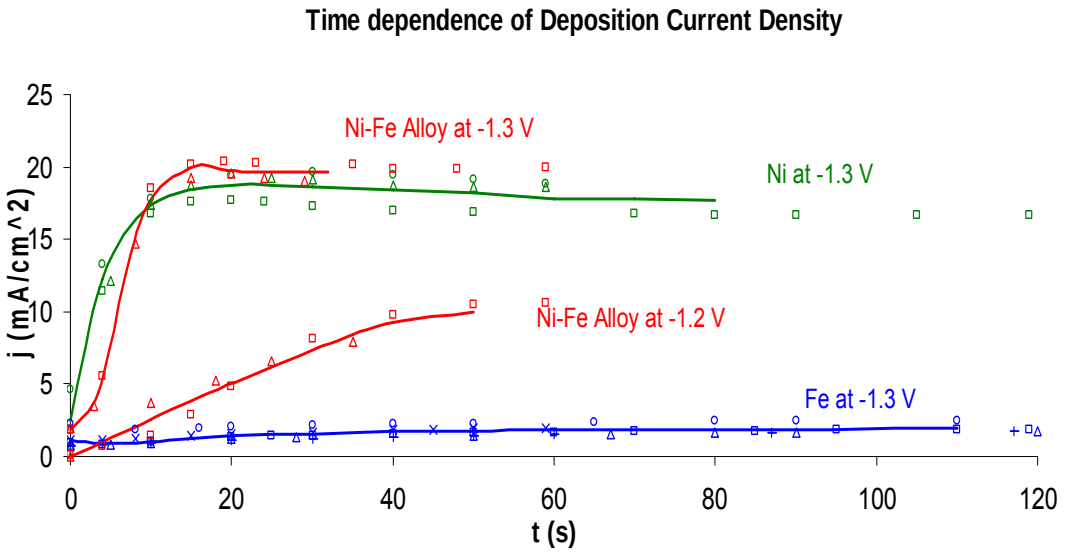

Figure 10: Current density versus time for different alloy curves. These curves can help select a deposition rate for each metal. The solid curves are drawn as a guide to the eye [19].

current is read from an ammeter while the exposed area is measured before deposition. As can be seen in figure 10, deposition rates can have dynamic changes by changing the applied potential on the silicon substrate. Changing the potential from -1.3V to -1.2V for a nickel-iron pellet changes the deposition rate from a nearly constant 20 mA/cm^2 to a time varying concentration increase.

These curves can be used for individual metals to use for codeposition. In this case we would use the deposition curves as our guide and chose these settings for each metal in the bath, since these curves were repeatable with different areas exposed.

2.2. Sample Characterization

2.2.1. Low-Energy Electron Diffraction

One method to characterize the sample surface is by using Low-Energy Electron Diffraction (LEED). A LEED spectrometer consists of a low-energy electron gun, multiple grids, and a phosphor screen. The electrons from the gun strike the sample at normal incidence and backscatter electrons excite the phosphor screen. By having low energy electrons, the LEED is surface sensitive. For example, a typical LEED pattern has electrons with energy of 50 eV. The wavelength can be calculated from the following equations:

$$p = (2mE)^{1/2} = 3.8 \times 10^{-24} \text{ kgm/s} \quad (12a)$$

$$\lambda = h/p = 0.17 \text{ nm} \quad (12b)$$

where m is the mass of an electron and E is the electron energy.

This wavelength is comparable to the lattice spacing in most metals (on the order of angstroms), therefore energies around 50 eV should be used to find LEED patterns.

Electrons diffract off the sample and scatter obeying the condition:

$$a(\sin\theta_n - \sin\theta_o) = n\lambda \tag{13}$$

where a is the lattice spacing between scattering, θ_n is the reflected angle from the lattice, θ_o is the incident angle, n is an integer and lambda is the electron wavelength. This form is also referred to as Bragg's law for scattering. As we i increase the energy of the electrons, the wavelength decreases and thus the angle decreases for scattering. When looking at the screen, the lattice is seen in reciprocal space. We can rewrite the diffraction law in reciprocal space as:

$$(\sin\theta_n - \sin\theta_o) = \lambda(ha_1^* + ka_2^*) \tag{14}$$

where h and k are integers corresponding to the reciprocal lattice and a^* is the reciprocal lattice vector.

A pattern of spots appears on the screen, which is a representation of the lattice structure. Since some lattices such as silicon have translational or rotational periodicity, repeated portions of the pattern can be observed by increasing the electron energy. Such an example of a 2x1 pattern is seen in

figure 10. Figure 10 is a picture of the LEED pattern of silicon <100> is shown after heating 15 hours at 650 degrees Celsius followed by a short anneal at 1250 degrees Celsius [22]. A full explanation of how LEED works and how many different patterns can result from different lattice structures is found in a paper by Heinz [23].

2.2.2. Reflection High Energy Electron Diffraction

Another method used in the characterization of samples and growth is Reflection High Energy Electron Diffraction (RHEED). The advantage of RHEED is that not only can we detect the quality of the surface due to a small penetration depth of electrons at grazing angles, but also we can count the number of atomic layers deposited in layer-by-layer growth.

RHEED works similarly to LEED, however instead of having grids to remove inelastic scattered electrons, the scattering is purely elastic by scattering at small angles and high energies. Electrons from an electron RHEED gun are scattered off the sample at angles ~ 2 ^{o} from the surface of the sample.

This geometry allows us to monitor the diffraction spots during growth, compared to LEED. These spots will oscillate in brightness depending on if there is a complete layer or partially complete layer during growth. A schematic of this process is shown in figure 12. The specular or central spot is used in my experiments measure the RHEED oscillations. This change in brightness is too difficult to quantify by hand, so instead they are measured using a charged-coupled display (CCD) camera. This camera can collect the intensity of light seen

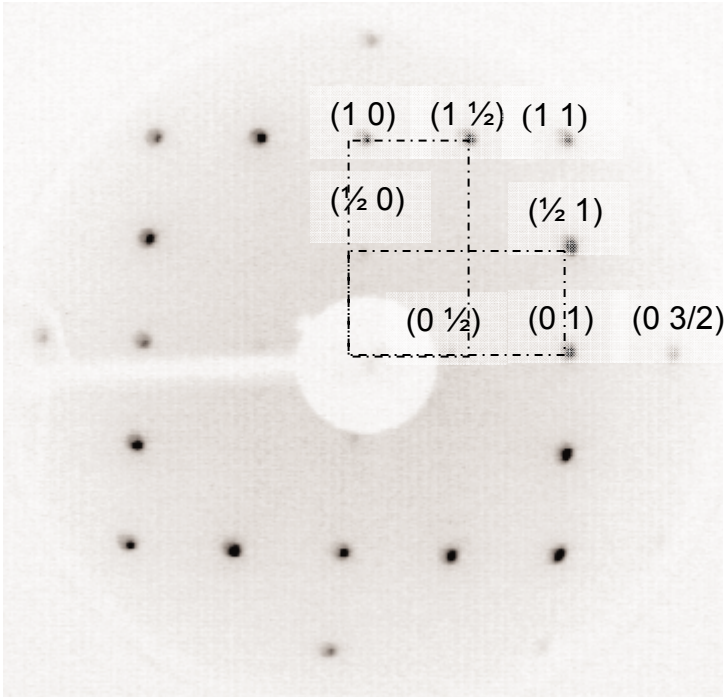

Figure 11: LEED pattern of Si(100). We note the 2x1 pattern when cleaned. Reproduced from [22].

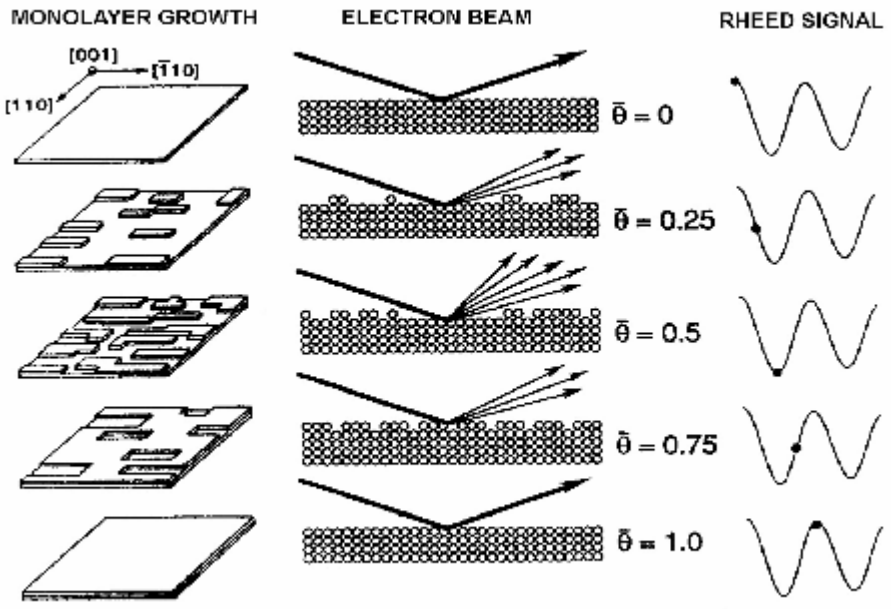

Figure 12: RHEED oscillation schematic showing one oscillation per monolayer. Reproduced from [24].

on the screen and measure quantitatively how bright each spot is. This is how each oscillation is measured as the sample grows each layer.

2.3. Superconducting Quantum Interference Device (SQUID)

In order to measure magnetic hysteresis loops of the sample, we use a superconducting quantum interference device (SQUID). SQUIDs are sensitive magnetometers that are based on superconducting loops containing Josephson junctions (JJ) [25]. Josephson junctions have a thin insulating barrier sandwiched between two weakly coupled superconductors. Instead of only electrons tunneling, Cooper pairs or bound electrons tunnel through this insulating barrier. The rate of tunneling is dependent on the size of the junction, namely an exponential decrease with distance.

Quantum mechanics determines the rate of current is a function of the phase difference. If we only consider real wavefunctions and boundary conditions, a current is detected across the junction regardless of applied external voltage. The equation governing this is:

$$I_s = I_0 \sin (\phi_1 - \phi_2) = I_0 \sin (\delta) \qquad (15)$$

If an external dc voltage is applied, an ac current is generated of the form:

$$I_s = I_0 \sin (\delta + 2\pi ft) \qquad (16)$$

where f is the quantum mechanical (deBroglie) frequency, which corresponds to the exact energy of a Cooper pair at the external voltage. [26] SQUID can

measure very small magnetic fields, 10^{-14} Tesla, and measure in a wide range of temperatures from 4 Kelvin to a couple hundred degrees above room temperature.

2.4 Hysteresis Loop

2.4.1. Properties of a Hysteresis Loop

Hysteresis is a process in which there can be different results based on initial conditions. Consider a step function centered at the origin as shown in figure 13. When the applied magnetic field is positive at zero Kelvin, the system immediately responds and all the moments align. When a small negative field is applied at zero Kelvin, the system responds with a negative magnetic moment. At zero field the sample could be either non magnetized or magnetized in either direction depending on the prior field direction. This uncertainty as to which state the magnetization of the sample is a property of the material known as hysteresis.

Consider hysteresis loops taken for two samples grown by electrochemical deposition together with an undergraduate researcher, figure 14. These samples were measured using SQUID (see chapters 4 & 5 for more data performed by SQUID). The first difference noticeable is that both of these are open loop curves. Applied fields below saturation now have multiple possibilities for how the sample is magnetized.

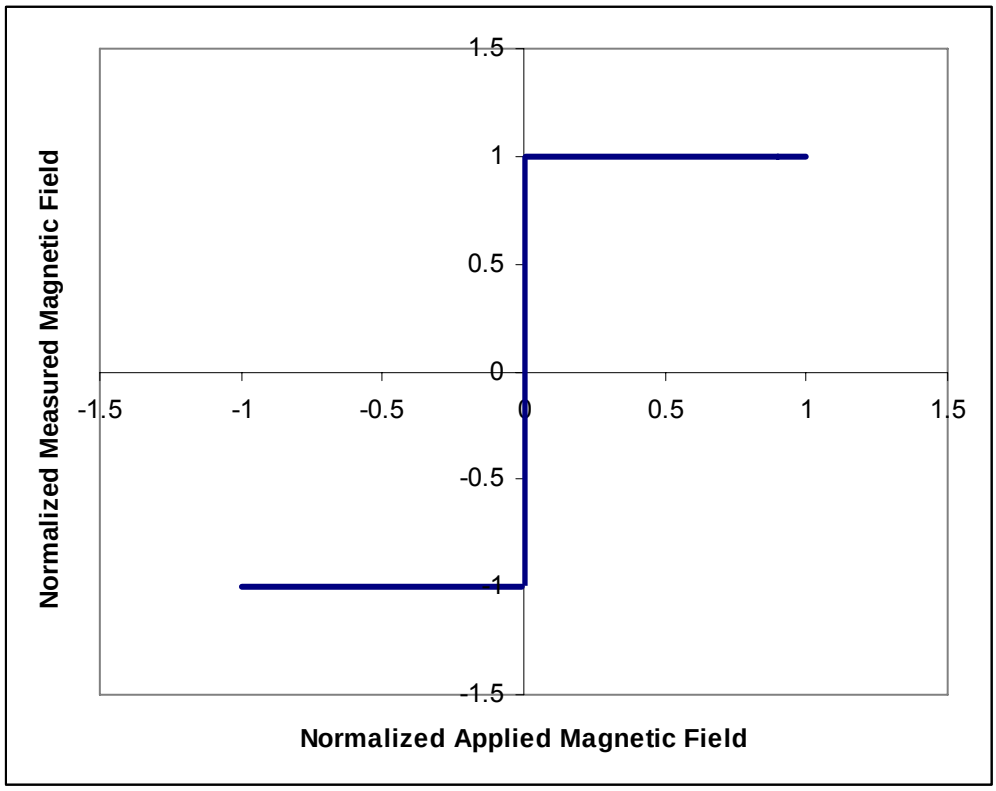

Figure 13: Normalized measured magnetic field vs. normalized applied field sketch. Given a small field in either direction produces a saturation of the sample (all moments are aligned).

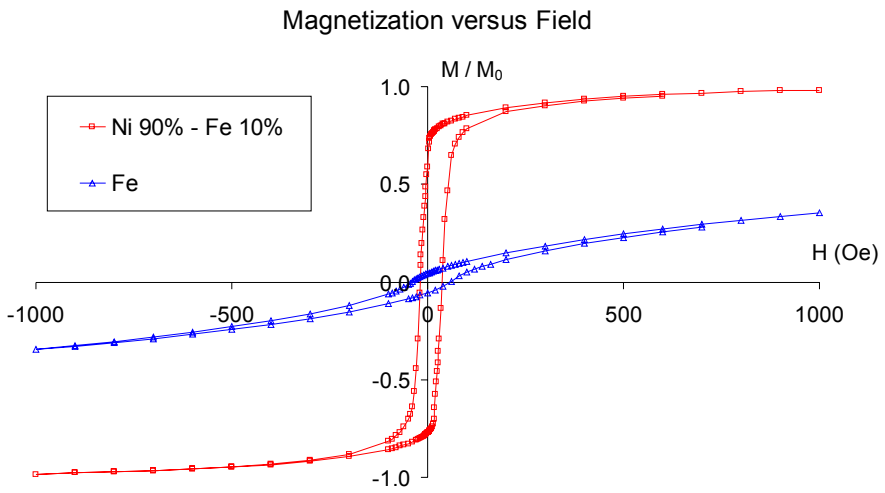

Figure 14: Hysteresis loops taken by a Superconducting Quantum Interference Device (SQUID). We note the high saturation magnetization and lower coercivity of the mostly nickel sample compared to the iron sample. [19]

Properties of hysteresis loops can now be defined based on these curves. The coercive field is a measure on the x-axis of how strong a magnetic field must be to measure zero magnetization on the sample. The remnant magnetization is the magnetization at zero field. Saturation magnetization is defined as maximum magnetization achieved. Coercivity is defined as the slope of the curve at zero field (dM/dH at H=0, more on this later). Magnetic work can be defined simply as the area under the curve.

Magnetic hard drive storage is a field concerned with the hysteresis loop of materials. It is important in this industry to know the difference between a 1 and 0 (on and off) and also what was already there (which point on the loop). To overcome this in the magnetic recording tape industry, the system is overdriven to a known state so we know which direction the loop is going. Because of this, it is important to minimize energy loss, so materials with a low coercivitiy and small magnetic work are desirable. After analyzing our data, the $Ni_{90}Fe_{10}$ loop is a much more suitable device for magnetic hard disk storage. In fact, many in industry use permalloy ($Ni_{65}Fe_{35}$) which is closer to our $Ni_{90}Fe_{10}$ than our pure iron sample.

2.4.2. Exchange Bias

Hysteresis loops of ferromagnetic films often look symmetric about their axes. This is not always the case when introducing antiferromagnetic material into a ferromagnet. The antiferromagnetic material is not easily influenced by an external magnetic field while a ferromagnet is easier to flip from an external

magnetic field. A shift in the hysteresis loop occurs due to coupling between the ferromagnets and antiferromagnets at an interface between layers of them. [27] [28]

Exchange bias can also occur by mixing ferromagnets and antiferromagnets such as nickel and manganese respectively. The hysteresis loops will simply be shifted by the field it would take to break down the ferromagnetic/antiferromagnetic coupling and allow switching from one applied field direction to the other.

2.5. Synchrotron Radiation & Photoemission

When charged particles are accelerated, electromagnetic radiation is radiated tangential to the path. In a synchrotron, electrons are accelerated in a circular path through the use of bending magnets. One advantage of using a synchrotron for our experiments is the higher brightness and intensity produced than traditional x-ray tubes. Most importantly, the energy of outcoming photons is tunable in energy and wavelength by the use of a monochromator. Energies of the outcoming photons can be as high as the kilovolt x-ray energies (keV).

For my research I have been using a third generation synchrotron, the National Science Foundation's Synchrotron Radiation Center's (SRC's) Aladdin. What sets apart a third generation source from previous generations is the use of wigglers and undulators. These devices are installed on the straight sections of the synchrotron and used to generate even stronger intensity radiation by wiggling the electrons many times over the path. On the curved paths, the radiated energy or photons are sent through mirrors and gratings before using

them at an end station. There can be multiple end stations for use at one bend in the synchrotron.

Incoming photons are absorbed in the sample, causing electrons to be promoted to higher energy states. In a photoelectron spectroscopy experiment, the electrons that are ejected from the lattice are collected. These electrons give us information on the magnetism at the atomic level.

The incoming photons have polarization associated with the beam. The center of the beam is linearly polarized while the top and bottom parts of the beam are right and left handed circularly polarized. The polarization of the beam can be selected through the use of baffles. Approximately 85% of the beam can be of the preferred polarization at the SRC [29].

2.6. Magnetic Circular Dichroism

The technique of magnetic circular dichroism (MCD) is a well-established method for monitoring the local magnetic behavior of atomic moments [30]. In order to establish chirality for the MCD experiment, one method is to have two different polarizations of photons, right and left, strike a magnetized sample. By taking a difference between these two spectra, a core level signature results that is unique to the sample. This difference is referred to as the x-ray MCD signal [31].

Another method is to fix the polarization of the incoming photons and change the direction of the externally applied magnetic field on the sample by 180 degrees. A schematic of the experimental geometry is shown in fig. 15.

The MCD signal is a spectral broadening of core level states. In our experiments, photon energies are chosen around 1 keV to probe to 2p level of our magnetic metals. This 2p level is spin orbit split into a j = 3/2 and j = 1/2 state. This is further Zeeman split by applying a magnetic field into the 6 2p-level electron states, 4 from the j = 3/2 state and 2 from the j = 1/2 state. We do not have the sensitivity to probe each individual electronic state, however we can probe the convolution of these states to see magnetic effects on the 2p level.

The spectra are obtained by using a total electron yield technique (TEY) [32]. TEY involves measuring the hole current instead of the ejected electrons. When an electron is ejected, a hole is created. The holes have the same magnetic properties as the ejected electrons. By measuring the current of these holes simply with a meter off the conducting sample arm, knowledge of the ejected electrons can be achieved.

Scans need to be normalized after taking them. They are normalized to the incident photon flux and mesh currents. The photon flux decreases over time during the scan. Because of this, the data will have higher counts at the beginning of the scan than the end. By dividing out the photon flux, the scans are calibrated. Also the mesh current is a measure of the amount of photons that directly go into the beamline. By dividing this out, a more accurate reading is achieved. Lastly, inelastic scattering and electrostatic screening need to be

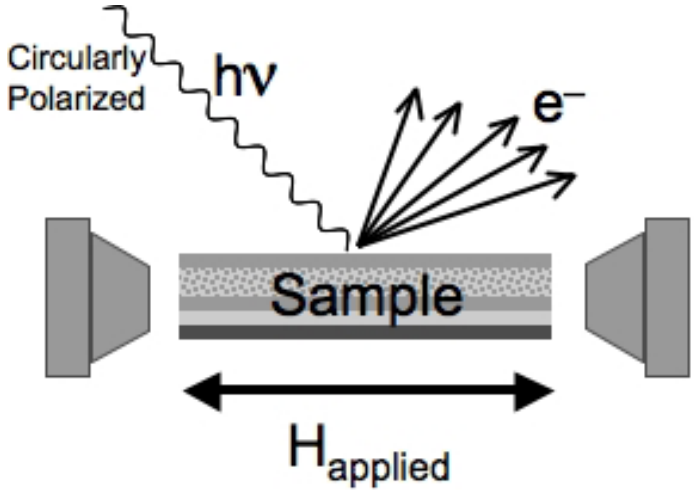

Figure 15: Experimental geometry for MCD. The applied magnetic field is fixed either to the left or right while circularly polarized photons interact with the sample. Electrons are ejected and the remaining holes are collected.

subtracted off the spectrum. As suggested by Janke-Gilman [33], a Doniach-Sunjic background subtraction was used [34] because of the asymmetrical lineshape that works well for x-ray photoemission multiple-scattering processes that occur.

2.7. Spin Glass

Magnetic frustration is a key component to the spin glass. Consider a lattice of spins where only a fraction of spins are located on lattice sites. Figure 16 shows two magnetic systems. Figure 16a shows three magnetic spins all pointing in the same direction. The coupling is positive between each magnetic spin. Figure 16b however shows a magnetically frustrated system. Each of the spins shown wants a negative coupling constant from their next nearest neighbor, however this spin cannot satisfy both demands to minimize its energy [35]. This frustration is due to its geometry and is typical for compounds with a Kagome lattice, figure 16c [36].

Nickel manganese alloys have a frustration that comes from the disorder from the interactions. Consider this alloy at zero Kelvin. The host nickel has 60% of its lattice sites with a magnetic moment. Adding an antiferromagnetic material such as manganese produces choices as to how the magnetic spin aligns in the lattice. One possibility is that the nearest neighbors of a magnetic spin are ferromagnetically aligned while two of the next nearest neighbors are antiferromagnetically aligned. If the coupling of these two balances out, this magnetic spin is magnetically frustrated and unable to remain in the lowest possible energy state.

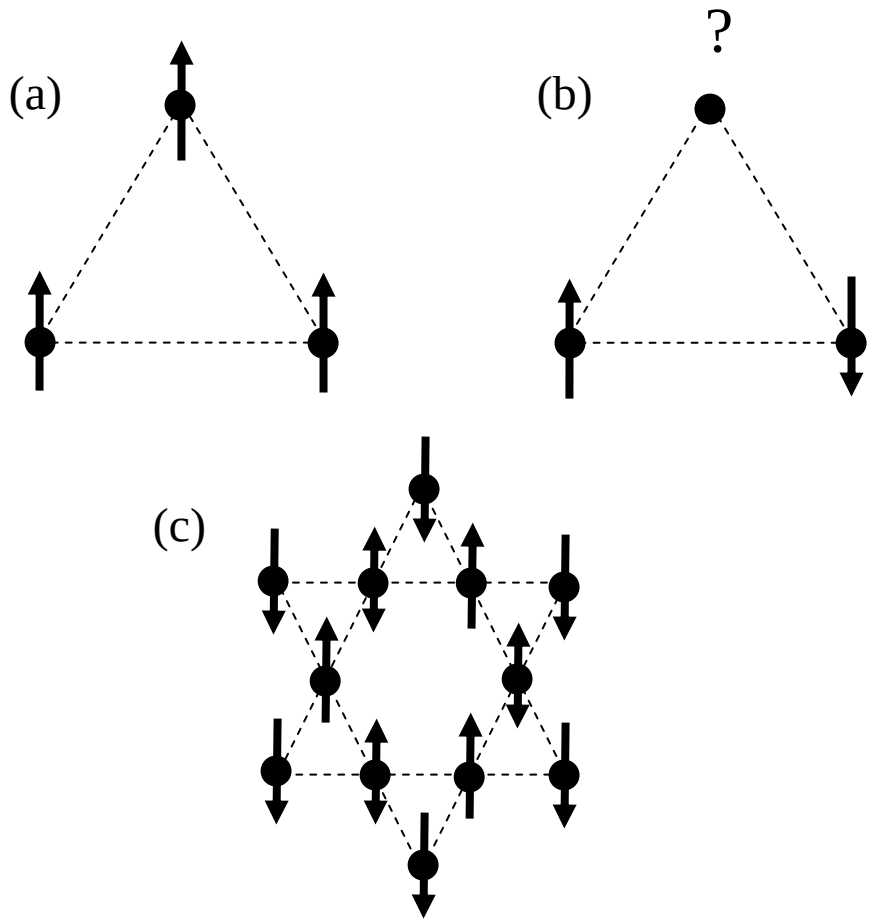

Figure 16: Example showing a lattice with no frustration, figure a, and with frustration due to the geometry of the lattice, figure b. A Kagome lattice is shown in figure c with alternating interior spins showing frustration (as shown with up/down arrows on same spin).

A spin glass usually starts out as a paramagnet well above the Curie temperature. As the temperature is lowered, the magnetization increases in an inversely-proportional fashion typical of the Curie law. As the temperature is lowered further, spins tend to form clusters which can rotate as a whole [37]. This continues until the spin glass approaches the freezing temperature, T_f.

As the temperature approaches T_f, the energy of the system decreases and the spins begin to interact over a longer range. The system tries to reach the lowest energy ground state by a variety of unknown transitions. In some cases the system can relax into a frozen state whereas other times the system can experience a random transition due to the random cluster formations. Below T_f, the system freezes into an amorphous spin state due to the inherent spin frustration mentioned earlier.

Most of the research to date that has been done on spin glasses are by doping an antiferromagnet such as manganese into a non-magnetic host such as copper or silver. This is shown in figure 17a. The magnetic spin coupling only occurs between the antiferromagnetic pairs which begin to see each other at very low freezing temperatures (~ 10 K). We investigate doping an antiferromagnet, manganese, into a sea of itinerant ferromagnetic spins, nickel. This is shown in figure 17b. The coupling now occurs not only between the antiferromagnetic spins, but also to the ferromagnetic sea surrounding them. We predict a much higher freezing temperature due to this stronger coupling.

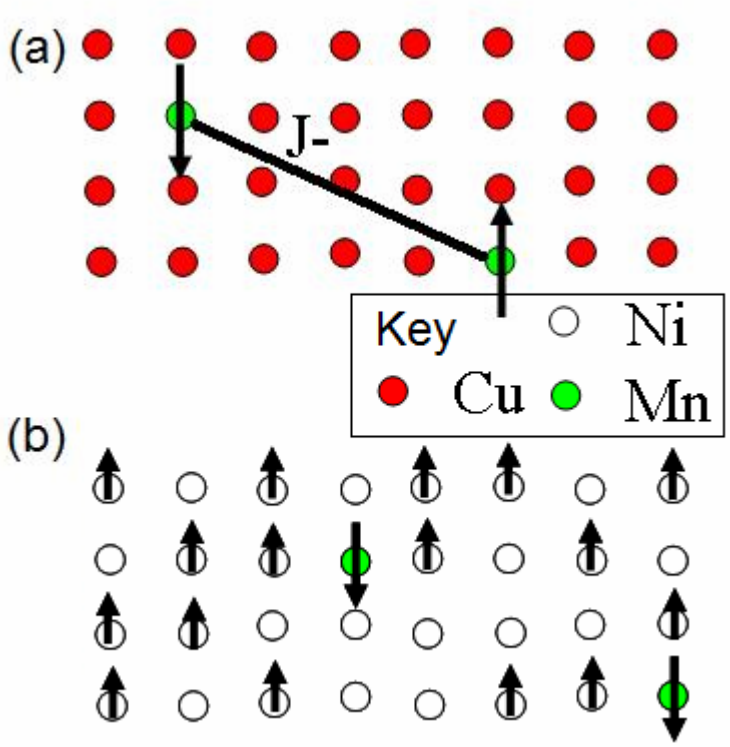

Figure 17: Cartoon sketch of (a) antiferromagnet (dark circle) doped into a nonmagnetic (gray circle) material, showing antiferromagnetic coupling and (b) antiferromagnet (dark circle) doped into sea of ferromagnetic (white circle) spins, where coupling occurs between any pair of magnetic spins.

Chapter 3

Spin Scattering Experiments……

3.1. Spintronics & GMR Background

Spintronics has a wide scope of interest and applications [38]. Spintronics is a subdiscipline of nanotechnology where spin currents replace electric charge as currents. These spin currents use multilayer structures as a filter to switch between high and low spin currents. Giant magneto-resistance (GMR) is a multilayer valve that has high or low resistivity depending on the direction of an external magnetic field. This effect recently won the Nobel Prize in Physics this past year, 2007 [39].

A simple model of a GMR device has two ferromagnetic layers separated by a nonmagnetic spacer layer. When the ferromagnetic layers have their magnetization directions parallel, current is allowed to flow through the device. However, if the ferromagnetic layers' magnetization are aligned antiparallel, most electrons traveling through are scattered, giving a much higher resistance. This current is directly related to the mean free path of the electrons through the material, λ [40]. There has been considerable interest in studying the mean free path of majority and minority spin carriers [41] [42].

One method to increase the GMR effect is to improve the spin-dependent scattering. By increasing impurities to the ferromagnetic layers, scattering can be

promoted and result in a higher GMR effect. If too many impurities are added, transmission current can decrease and thereby lower the GMR effect.

Therefore it is of interest to study the band structure where the magnetism plays a key role [43]. The sp bands have a higher group velocity, but it is the d bands that have the larger magnetization. The sp bands hybridize with the d bands near the Fermi energy [44], resulting in a measurable magnetic splitting [45]. Therefore, it is of interest to study these sp-hybridized bands and understand how the magnetism relates to spin scattering in these bands.

3.2 Theory of Band Filling

Ferromagnetic behavior results from how the bands are filled. As the 3d shell fills with electrons two types of electrons occur, namely those that will naturally align parallel to an external field and those that will align antiparallel to an external field. These are called the spin majority and spin minority bands respectively. When applying a magnetic field to a paramagnet at absolute zero, the spin minority electrons are raised higher in energy and the spin minority electrons are lowered in energy. This energy difference is $2\mu B$, resulting in a ferromagnet.

Remnant ferromagnets such as nickel have a band structure shown schematically in figure 18. In figure 18a, nickel is above the Curie temperature (627 K) has a net magnetic moment of zero. This is shown in the band filling

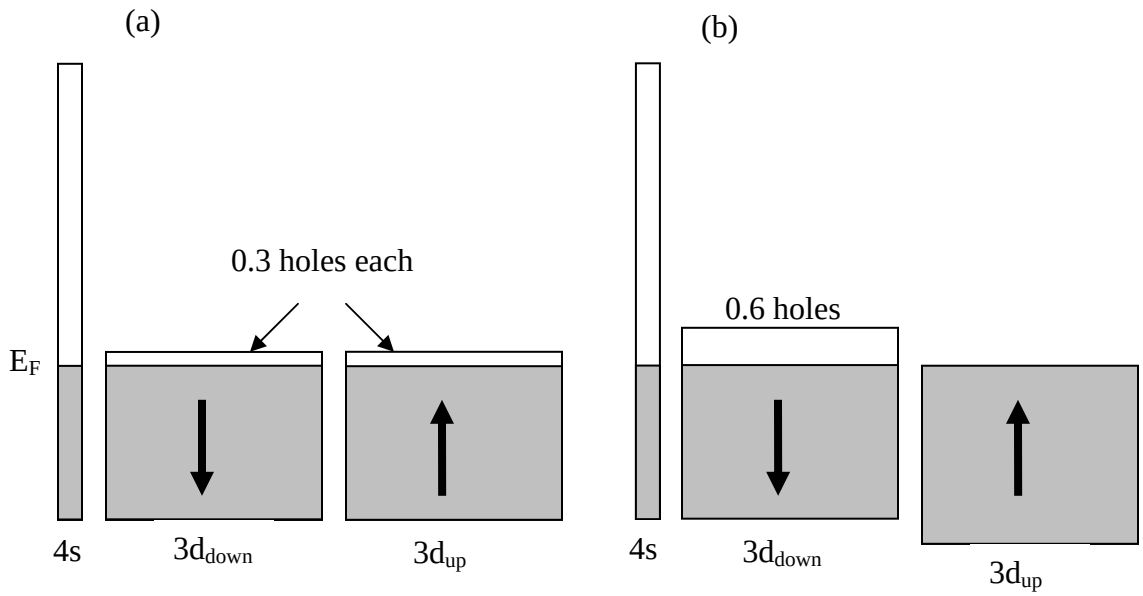

Figure 18: Pictorial relationship for nickel (a) above the Curie temperature showing how the band filling results in zero magnetic moment and (b) at 0 K showin a net magnetic moment resulting from holes in the spin minority band. Redrawn from [46].

having equal spin majority and spin minority carriers above the Fermi energy. However, if we are to cool the sample to 0 K, the spin majority fills up, leaving an excess of 0.6 holes in the spin minority that are unmatched. The magnetization of nickel arises from these spin-polarized holes in the spin minority band. [46]

3.3. Previous Work

Previous work in our group has been done on differentiating copper and nickels sp bands near the Fermi energy. In the first work, nickel, cobalt, copper, and permalloy ($Ni_{0.8}Fe_{0.2}$) were studied [47]. As shown in figure 19, the spin majority (up) and minority (down) peaks were imaged crossing the Fermi energy, 0 eV. These bands match well with theory developed by Bansil .[48]

Figure 19 shows the sp bands crossing the Fermi level. The exchange splitting is clearly discernable: about 0.6 eV in Ni(001), increasing to ~ 1.0 eV in 20% iron in nickel. We note that the intensity is not the same for each spin polarized spin majority or minority band. This is an indication that the lifetimes of spin polarized electrons in the spin majority or minority states are not the same and varies with alloy composition and material [49].

3.4 Preparation Chamber and Methods

For these synchrotron-based experiments, a different method of sample preparation and different chamber was used. Figure 20 shows a picture of this second preparation chamber, complete with evaporators on the right hand side and LEED on the left. A single crystal of nickel (110) was used instead of an

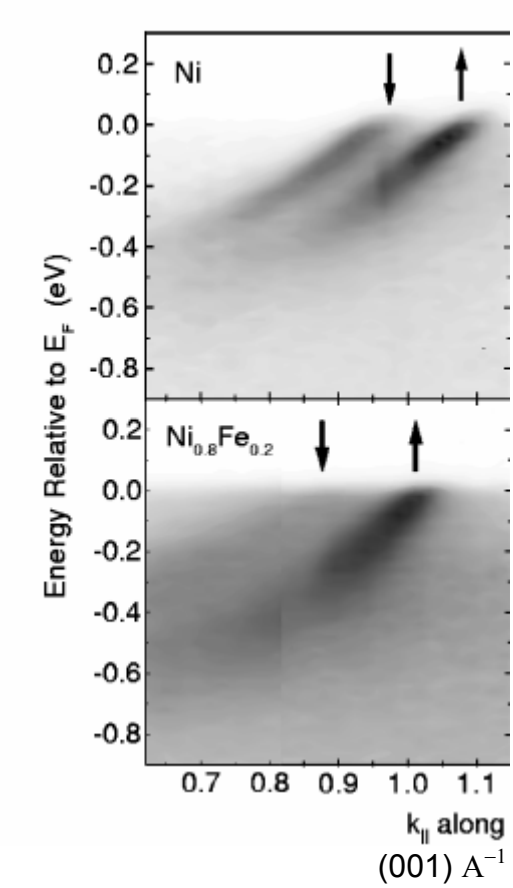

Figure 19: Nickel and iron doped nickel intensity plotted for energy vs. momentum (k). We note the strong majority and minority peaks that cross the Fermi level. Reproduced from [50].

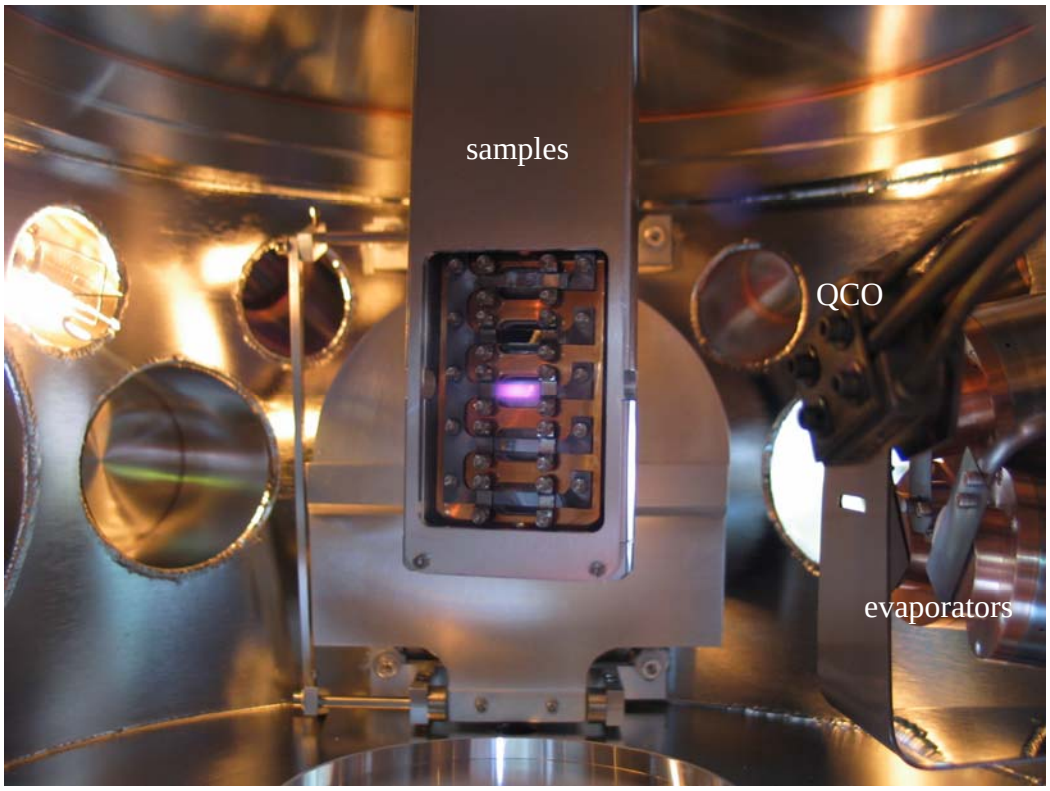

Figure 20: Sample preparation chamber used for spin scattering experiments at the SRC. In the center are up to five sample mounts. On the right hand side is a quartz crystal oscillator (QCO) and the sample evaporators. On the left hand side is a LEED to check crystal structure.

evaporated film to reduce scattering by defects, as reported by Gilman [33]. A small concentration of doping material is deposited onto 'perfect' single crystal surfaces using evaporators made in house. The sample is then heated to around 700 degrees Celsius to allow the top doping layer to diffuse into the surface layers of the substrate.

The concentration of the dopant is checked through atomic core-level scans. An example of a core level scan before the background was subtracted is shown in figure 21. This plot features two distinct peaks, one around 80 eV and the other around 100 eV. This corresponds to a nickel 2p core level and a manganese 2p core level. Notable are the two peaks that are merged in each larger envelope. The smaller peak (on the left) in the envelope is a convolution of the $2p^{1/2}$ level while the larger (on the right) is a convolution of the $2p^{3/2}$ level of nickel.

After a background subtraction, shown as a solid line, the area of each of these curves is taken. For this curve, it was determined that the manganese concentration is 7%.

3.5 Data Collection

My experimental results are compared to previous similar measurements performed by Altmann et. al [50]. In the latter experiment, a nickel host had impurities of chromium or iron diffused into the nickel. In our experiment, manganese is diffused into the host nickel. The sp-states of the nickel are

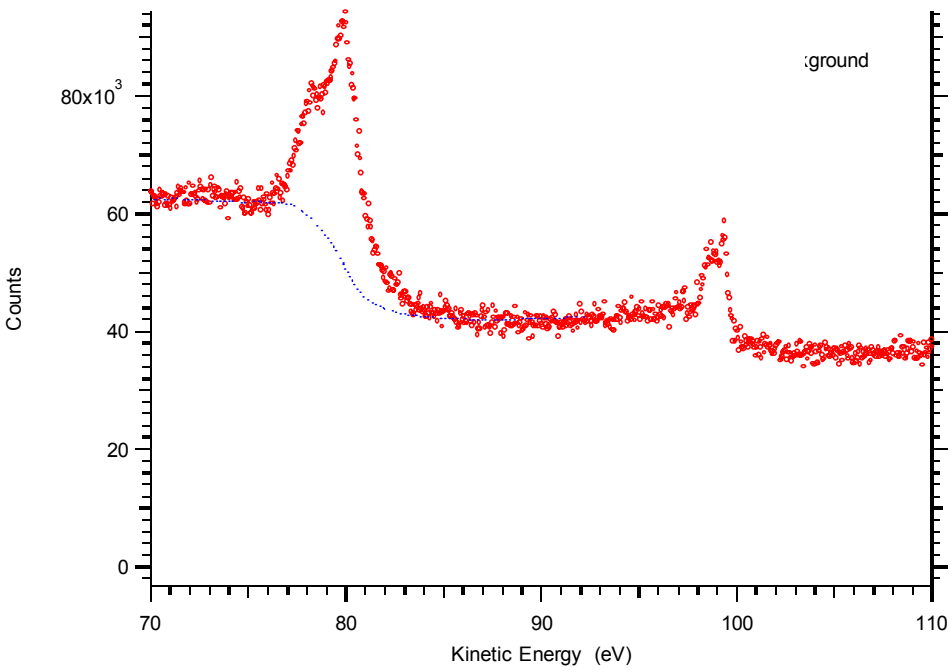

Figure 21: Core level scan showing nickel peaks around 80 eV and manganese peaks around 100 eV. The dotted line shows the Doniach-Sunich background that will be subtracted from the peaks.

measured in either case using an electron spectrometer with energy and angle (momentum) multidetection with p-polarized radiation, figure 19.

A sample scan showing energy versus parallel momentum is shown in figure 22. From this a slice through the Fermi energy at 22.42 eV is taken. We can see that the sp bands continue 0.15 eV below the Fermi energy to which they broaden out and become indiscernible. The spin minority channel (down) appears to get broader much more quickly than the spin majority channel (up). This is a sign that the manganese has strong ferromagnetic behavior in the sp bands, just like iron in figure 22.

Figure 23 shows a plot of the intensity of these states at the Fermi energy for several different lightly doped alloys of nickel. By adding iron into nickel, the spin minority peak decreases quickly while adding chromium causes both spin channels to broaden and move closer together in momentum space. By doping with manganese, a similar appearance to that of the chromium data is apparent, however the position of the peaks in momentum space remains constant.

Further analysis of this data follows in the next section. Figure 24 is a plot of changes in this data on diffusing manganese into nickel. As the doping concentration increases to 20 % manganese, the spin majority peak shown on the right decreases in intensity while the spin minority peak on the left increases slightly. The scatter in the data points for this figure are much smaller than the scale of the figure itself, hence no data points are shown.

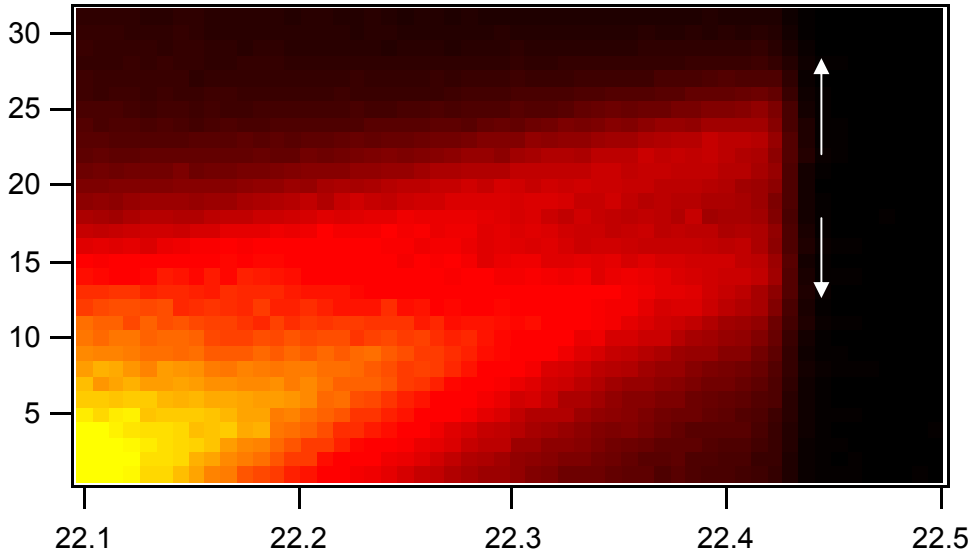

Figure 22: Momentum (arb. units) vs. energy plot (arb. units) for 7% manganese diffused into nickel. The color shows the intensity or number of photoelectrons. The arrows indicate the strong splitting between the spin majority (up arrow) and spin minority (down arrow).

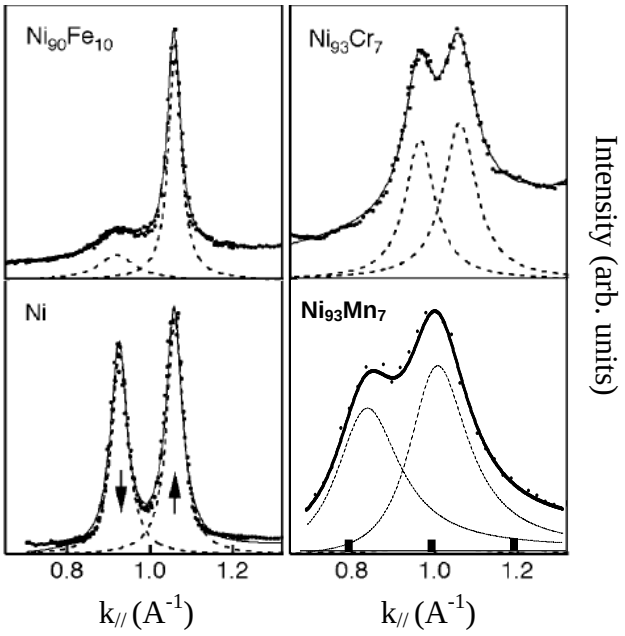

Figure 23: A plot of the parallel momentum distribution (100) vs. photoemission intensity as a function of magnetic impurity doping. Iron doped (upper left), chromium doped (upper right), undoped, and manganese doped (lower right) with nickel are shown. (All plots but manganese doped nickel come from [50])

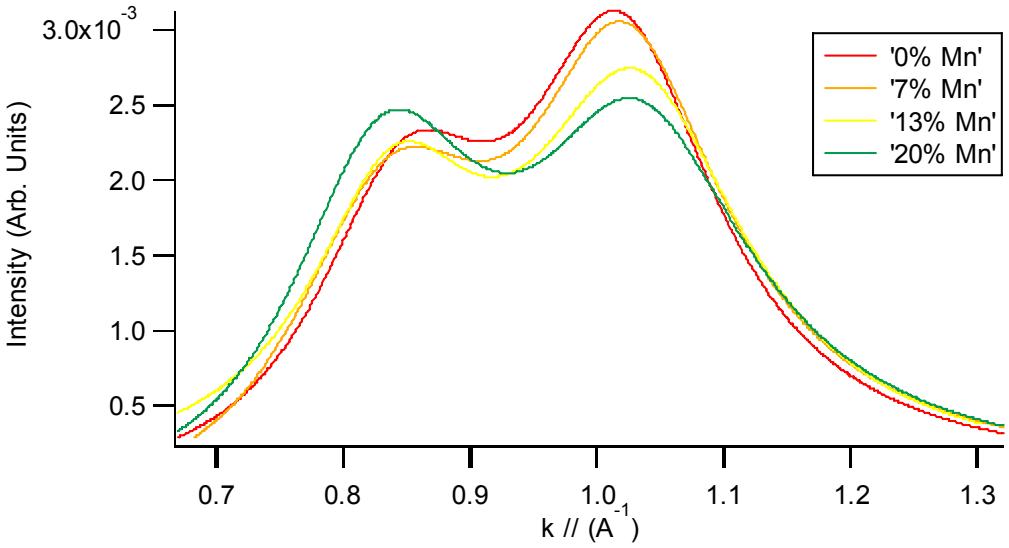

Figure 24: A plot of the momentum distribution vs. photoemission intensity as a function of magnetic impurity doping, specifically manganese. The spin majority peak, on the right, decreases in height with increasing concentration of Mn while the spin minority peak, on the left, increases in height with increasing Mn concentration.

The location in momentum space does not change for manganese diffused into nickel, although the peaks do shift slightly at different concentrations. I don't anticipate this shift as being physically significant to the changes in magnetism by adding more manganese into nickel. Unlike the drastic changes observed in figure 24, the changes observed in figure 23 show the ferromagnetic exchange-splitting remaining more or less constant, but with subtle changes in the scattering characteristics of both spin channels.

3.6. Further analysis of data

Many unique spin transport quantities can be extracted from these curves, figures 25 and 26.

The magnetic splitting exchange, or dk_{ex}, can be calculated by the difference in the Fermi wavevectors at the majority and minority peak heights. Figure 25a shows the results for two previously measured alloys along with the new data for manganese alloys. The magnetic splitting is "a measure of the difference in band filling i.e. magnetic moment." [50] The chromium exhibits this trend as we can see that the dk_{ex} decreases as the percent of dopant increases. This corresponds directly to the Slater-Pauling curve. Chromium is added in antiferromagnetically into the nickel and the magnetic moment decreases. According to our data, the iron does not change the magnetic moment of the nickel. One would expect, looking at the Slater-Pauling curve, that the magnetic moment would ferromagnetically enhance the magnetic moment. This however is not seen.

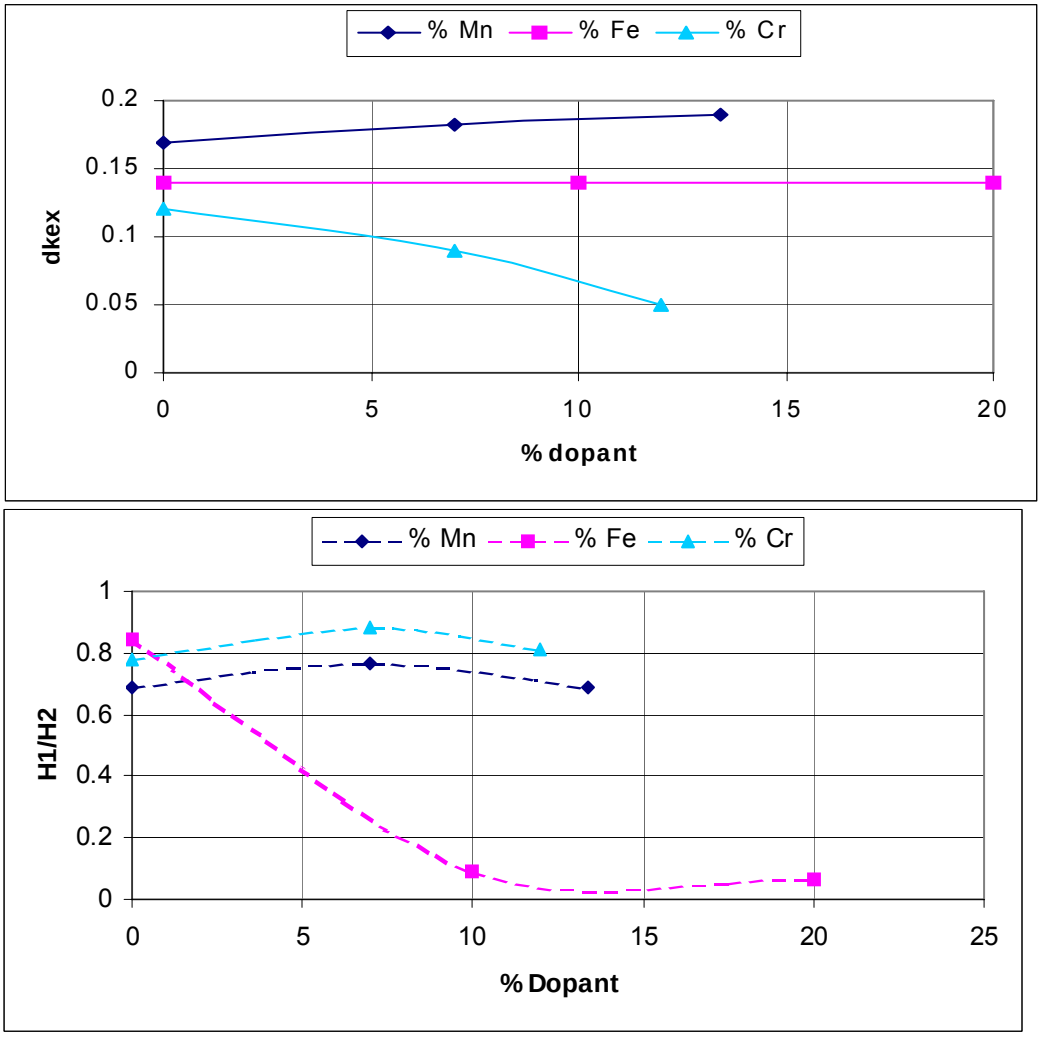

Figure 25: A comparison of spin scattering data for three different dopants, one of which (Mn) is new. In 22(a) dk_{ex} shows us how the bands were filled and is proportional to the magnetic moment. In 22(b), the ratio of peak heights (majority/minority) show us whether the spin majority (low ratio) dominates or the spin minority dominates (high ratio). The lines are drawn as guides to the eye. Data from Fe and Cr come from [50].

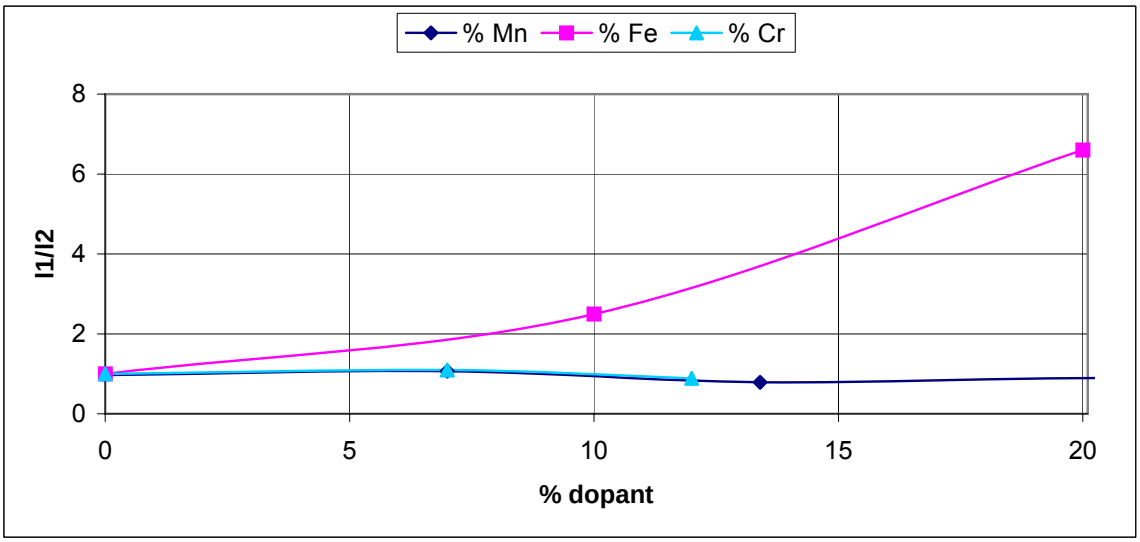

Figure 26: Ratio of the majority to minority mean free paths (l1/l2) versus dopant. We note that the manganese and chromium dopants do not change their widths while the iron widths, particular the spin majority, gets much broader with increasing iron concentration. Data from Fe and Cr come from [50].

The newest data, the manganese dopant, exhibits unusual trends. The plot of our data suggests a small increase in the local magnetic moment for small concentrations. This is seen in the Slater-Pauling curve. However at slightly larger concentrations the Slater-Pauling curve turns over and decreases the magnetic moment. We however notice a small increase. This increase shows that there is a ferromagnetic interaction between the nickel's sp-band with the manganese at these small concentrations, < 10% manganese in nickel.

Peak heights can show us the amount of filling in either the majority or minority carriers. The height ratio is taken to be the minority height over the majority height, as shown in figure 25b. This way the ratio should always be less than 1. In the iron doped nickel, we notice a sharp decrease in the ratio of the heights that corresponds to a collapse in the minority peak height. The Mn and Cr dopants both exhibit similar trends where the minority peaks do not disappear like the Fe dopant counterpart. This shows that the minority spin carriers play a significant role in the magnetism, meaning that as far as the sp-bands go, manganese is acting like chromium as a dopant.

Lastly, the mean free path l can be calculated from the inverse of the full width half max of each of the minority and majority peaks. A ratio of the resulting mean free paths is shown in figure 26. We note that the manganese dopant closely follows the chromium dopant while the iron dopant has a relative increase in the mean free path of the majority peak than the minority peak. The iron curves are seen to get broader and merge together while the relative widths of the chromium and manganese dopants do not change.

In summary, the manganese doped nickel looks very similar to that of chromium doped nickel, however there are differences. The manganese shows increased ferromagnetic order at low concentrations (< 10%) that chromium does not. Also the chromium peaks eventually merge together signaling zero ferromagnetism whereas the manganese peaks maintain a finite exchange splitting.

Chapter 4

Local and Nonlocal Magnetism of NiMn……

4.1 Background

Magnetic behavior in alloys is determined by two effects. The behavior can be 'local' by changing the magnetic moment or 'non-local' that results from the interaction between magnetic spins. Both characteristics change with concentration of manganese in nickel alloys. We monitor the former using magnetic circular dichroism (MCD) and the later shows up in the hysteresis behavior of the magnetization as a function of applied magnetic field.

4.2 Magnetic Circular Dichroism Introduction

The technique of magnetic circular dichroism (MCD) is a well-established method for monitoring the local magnetic behavior of atomic moments [51]. Measurements have been reported using MCD at the nanoscale, observing a spin reorientation transition in ultrathin films of nickel and its alloys, from in-plane magnetization to out of plane [52]. Also, temperature effects relating to the finite size effect [53] have been studied for these metals [54]. However, a study of nickel manganese alloys has yet to be explored.

Samples were measured with a 10m toroidal grating monochromator at the Synchrotron Radiation Center (SRC) in Wisconsin using a MCD chamber set-up initially by Harp [55]. Measurements are made at the L-edges of each element in the nickel-manganese alloy. The samples varied in composition of manganese in nickel protected by buffer layers of copper. The thickness of the nickel manganese alloys were 100 Å. The samples were cooled to 100 K during measurements. Since the probing depth of the x-rays is longer than 20 Å, and because of the elemental specific nature of MCD, copper layers makes no effect on the spectrum. The samples were not annealed to make sure copper does not diffuse into the nickel sample.

Signals were taken with the field parallel (σ^+) and antiparallel (σ^-) using total electron yield. These samples were thick enough to simplify the expression for the intensity of the scattered radiation to:

$$I \sim \sigma/\alpha \qquad (17)$$

where α is the total absorption coefficient at our photon energy. This absorption coefficient is estimated to be 20% due to the geometry of the experiment [56]. After background subtractions, fractional dichroism was determined from two scans, each for opposite field directions to establish the chirality of the measurement. The formula simplifies to:

$$\text{Fractional dichroism} = (I^+ - I^-)/(I^+ + I^-) \times 100\% \qquad (18)$$

This formula was used to analyze the six p-level state multiplets for the magnetic alloys.

4.2.1. MCD as a function of field

The first experiments performed were measuring each sample, at a particular concentration, as a function of the applied field. Figure 27a is a plot of the manganese peak's fractional dichroism vs. the photon energy. This sample has the best signal to noise ratio for manganese peaks measured. Even at small fields as low as 100 Oe, the manganese peaks have relatively the same shape. Manganese has a large magnetic moment, but is not high in concentration in this alloy. Therefore the response looks the same irregardless of field.

Calculations by Zeller show that the magnetic moment of Mn is less than the bulk value due to a developing virtual bound state (VBS) in the majority density of electron states [51]. This virtual bound state is one possible cause of the collapse in the magnetic moments of nickel, since it disturbs the density of hole states at the Fermi level (Stoner criterion). For more discussion about VBS, please see chapter 6.

Figure 27b shows the spectral changes in the dichroism signal in nickel as lower fields are used, from 1500 Oe downward. Nickel represents the majority of magnetic spins in the lattice and has a relatively small magnetic moment (0.6 μ_B/atom). This moment is 'itinerant,' the spin-holes hopping from atom to atom. In contrast, the manganese moment is fixed at the substituted lattice site(s). When the field is lowered, the nickel atoms are less likely to reorient themselves to

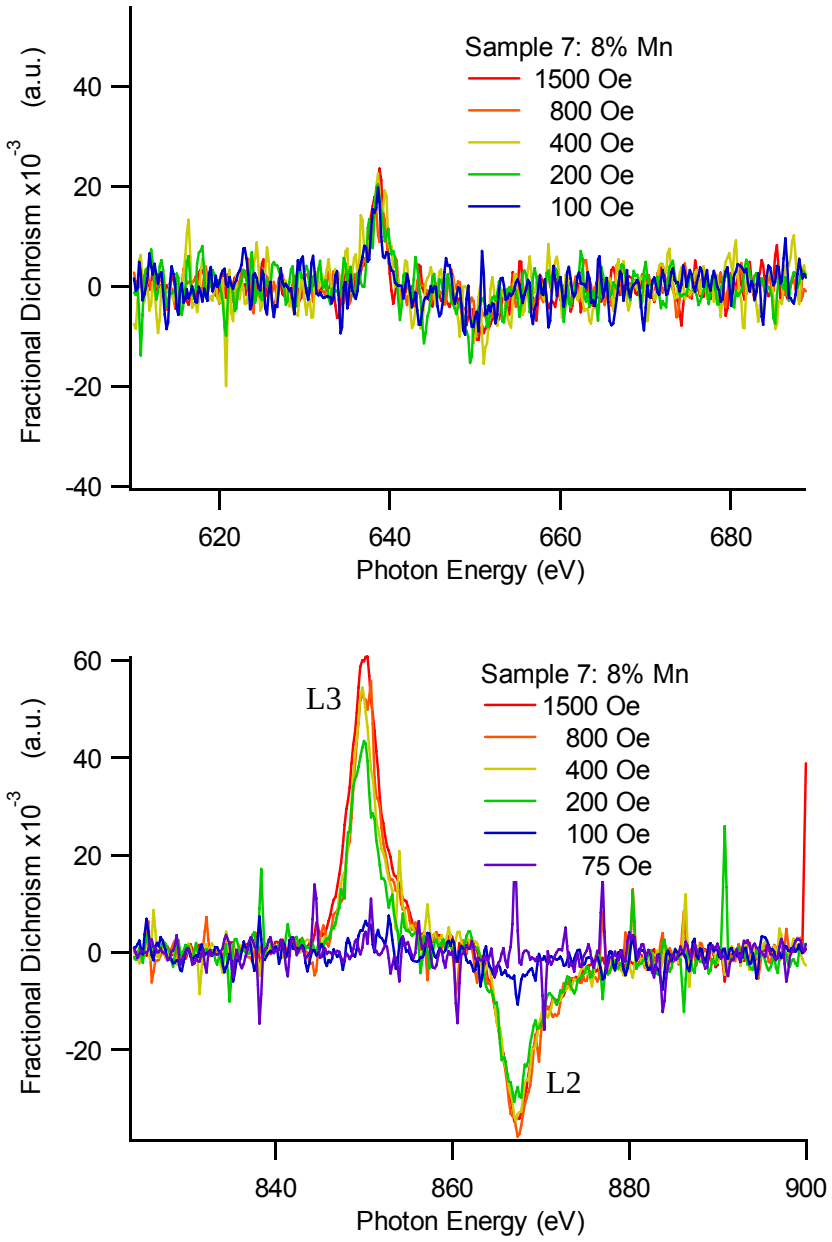

Figure 27: Fractional dichroism measurement of the (a) manganese peaks in a 8% manganese in nickel sample and (b) nickel peaks in a 5% manganese in nickel sample. We note the small signal to noise ratio that makes it difficult to discern any spectral changes.

fields in opposite directions. At larger concentrations of manganese, the manganese spins appear to influence the nickel spins, making even less nickel atoms reorient in the magnetic field.

Also noted is that each of these dichroism signals have the same up/down peak shapes. The up-peak is referred to as the L3 peak while the down-peak is referred to as L2. These peaks have the same polarity for both nickel and manganese, emphasizing ferromagnetic alignment at small concentrations of manganese in nickel. This is in agreement with a prior report for 2% Mn in Ni alloy [51]. This similarity of ferromagnetic alignment for the MCD signal has been discussed by Harp [57].

4.2.2. Calculations from MCD

Each fractional dichroism signal was normalized by dividing out the beam current and mesh current. The areas of the L3 and L2 curves of nickel, see figure 28, are used to calculate the ratio of the orbital to spin angular momentum using equation 19:

$$\frac{\langle L_z \rangle}{\langle S_z \rangle} = \frac{4}{3} \frac{\int_{L_2+L_3} dE\left(I^+ - I^-\right)}{\int_{L_3} dE\left(I^+ - I^-\right) - 2\int_{L_2} dE\left(I^+ - I^-\right)} \qquad (19)$$

where $\langle L_z \rangle$ is the orbital angular momentum and $\langle S_z \rangle$ is the spin angular momentum [58]. Our data determines that this ratio is a constant value of 0.235 for

% Mn in Ni	0	5	8	10	12	average
<Lz>/<Sz>	0.265	0.216	0.240	0.212	0.244	0.2354

Table II: Ratio of the orbital angular momentum (<Lz>) and the spin angular momentum (<Sz>) for each alloy of nickel manganese.

concentrations of Mn from 0 to 12% as shown in table I. This suggests that the nickel's contribution to the spin and orbital angular momentum remains constant. Also, the polarity of the dichroism shows that the nickel remains ferromagnetic, regardless of how much manganese is present from 0-12% at temperatures of 100K. This agrees with the fact there is no dependence on the 3d occupation number, n.

To calculate nickel's contribution to the overall magnetic moment, we calculate the orbital and spin angular momentum separately. Each contribution to the difference is used as a normalization factor to determine the angular momentum components. The net magnetic moment is then calculated using the formula:

$$\mu_{total} = -\mu_B\left(\langle L_z \rangle + 2\langle S_z \rangle\right) \qquad (20)$$

4.2.3. Discussion & Conclusions of Results

Spectral evolution with changing concentration at a maximum saturation field of 1500 Oe is plotted in Fig. 28a. At 5% of manganese in nickel, an enhanced dichroism signal on the nickel is noted. At higher concentrations, x > 10%, this nickel signal decreases. The peaks all have the same lineshape about the axis. An enhancement of the L3 and L2 peaks of the nickel progressing from 0% to 5% manganese in nickel is also noted. With increasing concentration, greater than 5%, we note a collapse in the spectral peak amplitude of nickel.

From these peaks we can calculate the magnetic moment of nickel using equations 19 and 20. The results are plotted, along with the Slater-Pauling curve,

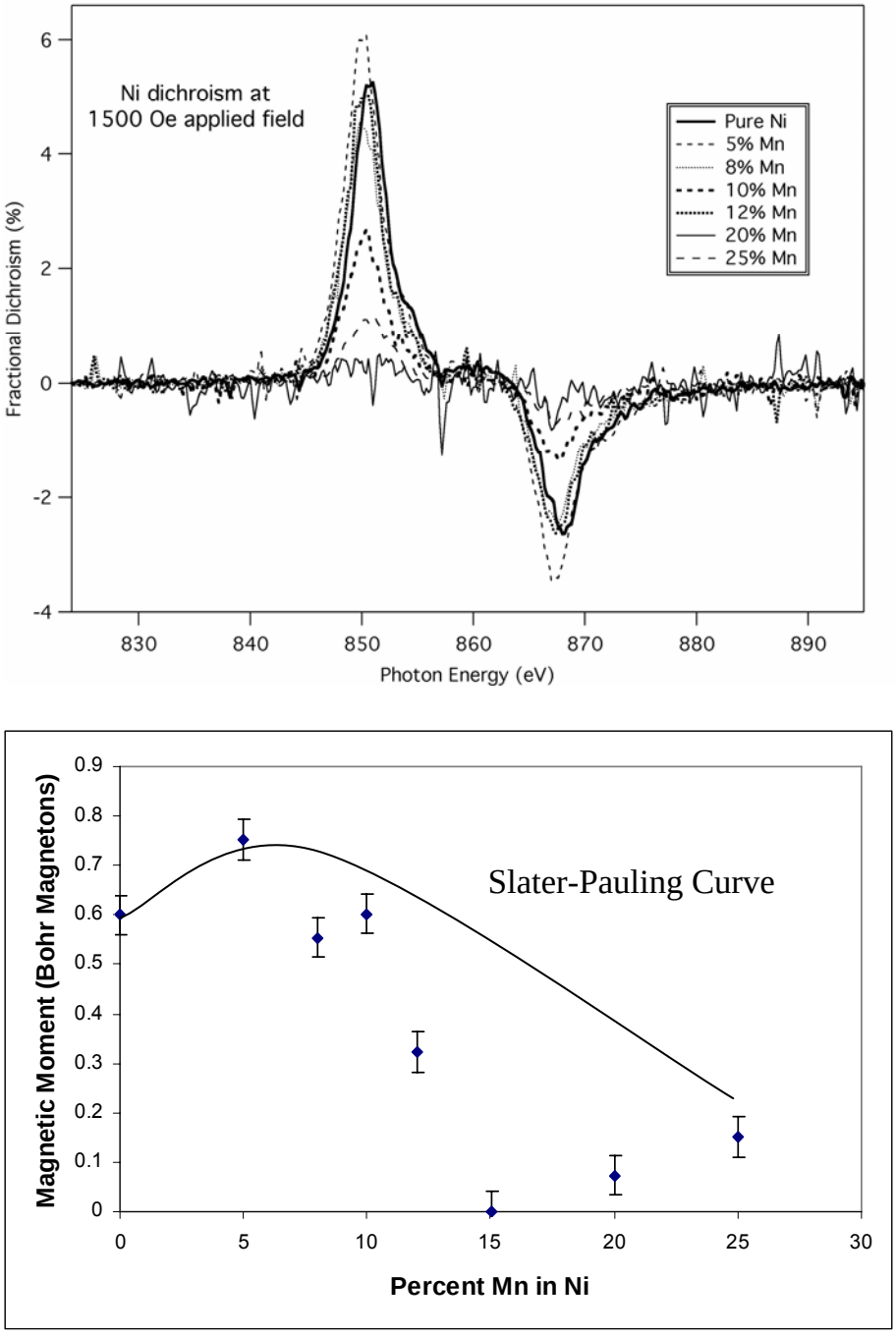

Figure 28: (a) Fractional dichroism of $Ni_{1-x}Mn_x$ for the L3 and L2 peaks of nickel. Using these peaks, magnetic moment of nickel is calculated and plotted vs. percent of manganese in nickel in figure 23(b).

in figure 28b. The enhancement of the moment at 5% manganese in nickel is seen in figure 28b. The nickel moments however for concentrations between 8 - 12% appear lower than the Slater-Pauling curve. This is because the manganese is becoming more prevalent and affecting the individual nickel moments, even though the ratio of the orbital to spin angular momentum remains constant for nickel.

Lastly, the transition into a new regime is seen where the magnetism goes to zero at 15% then recovers a small amount at 25%. This is called a 'reentrant spin glass' (RSG) phase. The transition from ferromagnetism below 15% and a reentrant spin-glass above 15% will be discussed in more detail in chapter 5.

4.3. Hysteresis Measurements

4.3.1. Hysteresis as a function of concentration of manganese

Hysteresis loops were taken with SQUID measurements to measure the non-local magnetization of the sample. The samples were a trilayer of films of copper, nickel-manganese, copper grown on silicon, as discussed in chapter 5. Scans were performed at 100 K for various compositions, since this is the temperature where the magnetic dichroism measurements took place in section 4.1. Fig. 29a is a plot of the hysteresis behavior for $Ni_{1-x}Mn_x$ for concentrations up to 15%. Fig. 29b shows hysteresis behavior at concentrations 15-25%. There is a drastic change in the hysteresis behavior as the concentration approaches 15%.

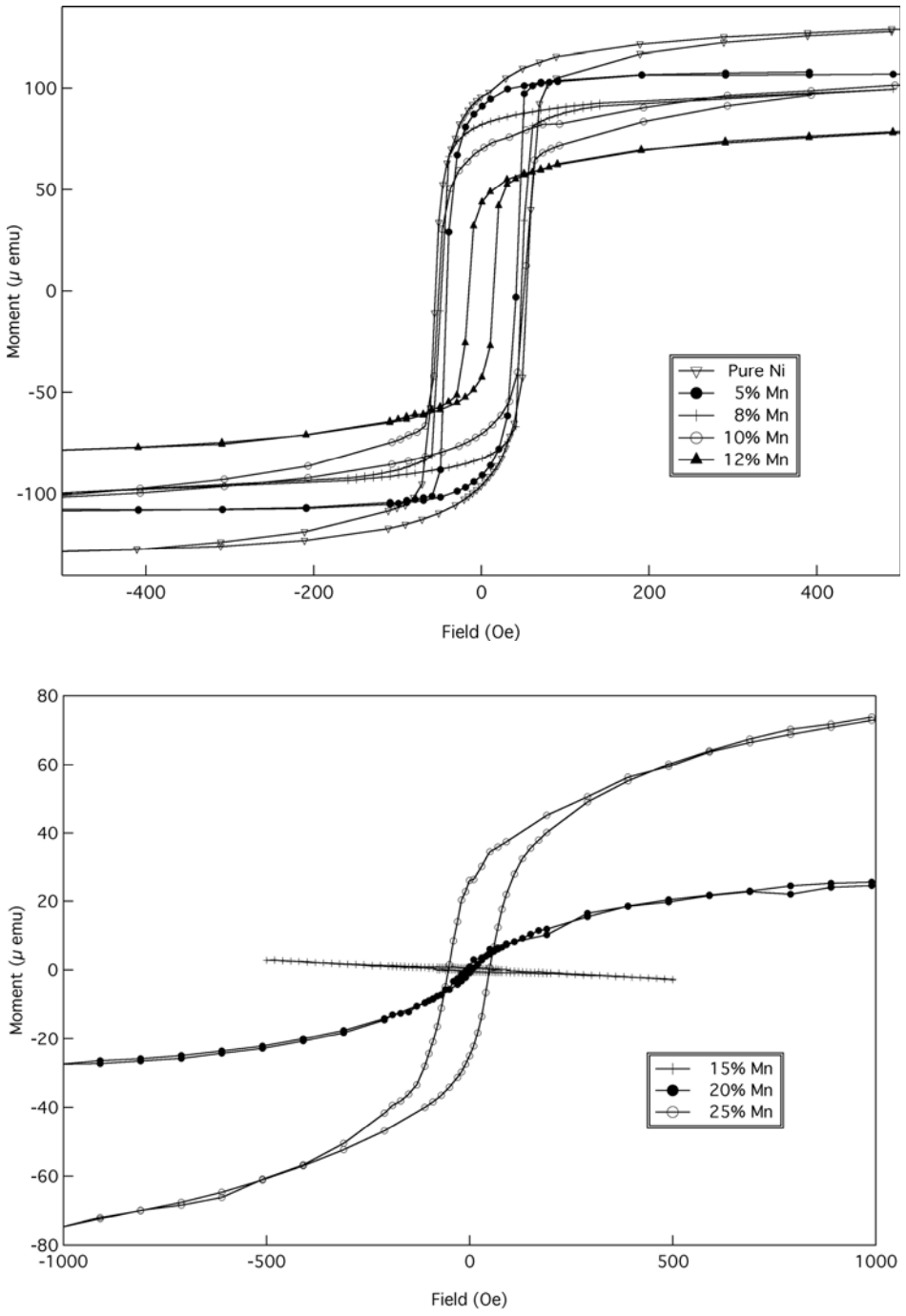

Figure 29: Hysteresis loops measured by SQUID at 100K where magnetization (emu) vs. applied field (Oe) is plotted. Although the saturation magnetization decreases with increasing concentration of Mn (just like T_C), the coercive field, Fig. 29a, remains relatively constant at low concentrations dropping off rapidly at x ~ 10%. Fig. 29b shows a drastic change in hysteresis behavior approaching a spin-glass concentration x ~ 25%.

The hysteresis loops drop to zero magnetization at 15% then rise back up toward the reentrant spin-glass phase near 25%.

The saturation magnetization parallels similar behavior to the MCD measurements. There is an enhancement of the saturation magnetization at 5% manganese in nickel, followed by a steady decrease to zero at 15% manganese. The coercive field is constant for alloys from 0-12% manganese in nickel. This shows that there are ferromagnetic interactions through this range. Both of these results are in good agreement with the conclusions from the dichroism results in section 4.1.

Figure 30 summarizes the variation of (a) the saturation magnetization and (b) coercivity as a function of Mn concentration. This data is directly extracted from figure 26. Figure 30a shows a decrease in the saturation magnetization, which mimics the T_C behavior for dilute $Ni_{1-x}Mn_x$ ($x < 15\%$), figure 3 [9]. The coercivity, figure 30b, behaves similarly, decreasing slowly at low concentrations before collapsing rapidly at concentrations $x \geq 12\%$, figure 29. This behavior suggests that, although the manganese-moments may first align with the nickel moments and the magnetization, they disrupt the overall spin order. This spin disorder shows a sudden increase for $x \geq 10\%$ and the onset of a reentrant spin glass phase, $x \sim 25\%$. This transition into a reentrant spin glass is characterized by a decrease in the local moments on both elements and a decrease in the non-local spin coupling, as suggested by the behavior of the coercivity, figure 30b.

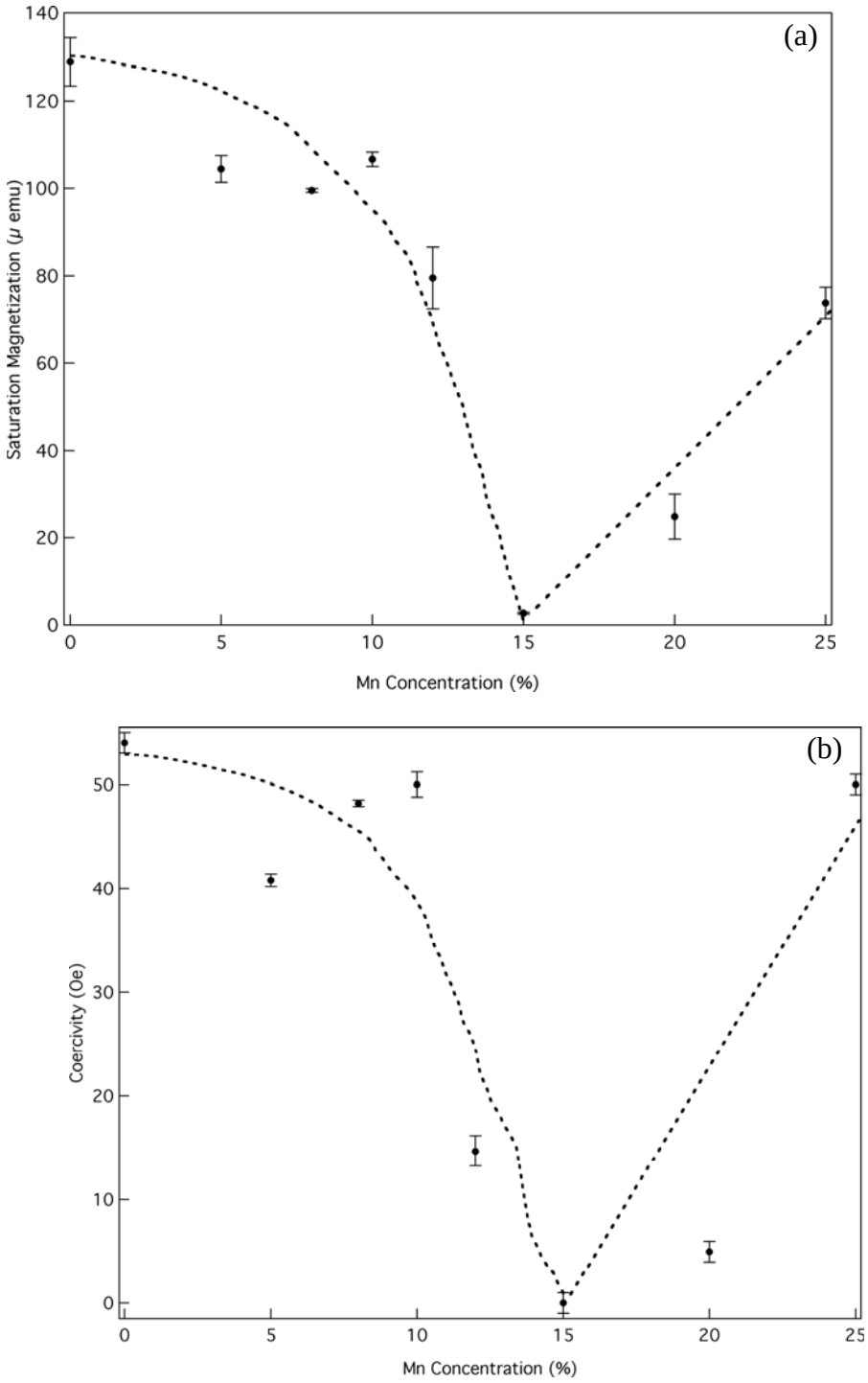

Figure 30: Curves showing the (a) saturation magnetization and (b) coercive field versus concentration. Note: the saturation magnetization M_S and the coercivity H_C both decline rapidly to zero at x ≈ 15%, then increase for higher concentrations. The line drawn through the data is a guide to the eye.

4.3.2. Temperature effects on hysteresis loops

As the temperature decreases for a ferromagnetic material, magnetic moments lock into their magnetic alignment, making it a slower process for all the moments to align by increasing the applied field. Hysteresis data is taken for ten percent manganese in nickel over a temperature range from 5 K to 300 K. Spectacular changes with temperature are shown in figure 31.

From these varied temperature hysteresis loops, many magnetic phenomena can be explored. The saturation magnetization remains relatively constant over the range of temperatures. This is encouraging, since the sample has the same concentration of magnetic materials throughout each hysteresis loop. The Neel temperature can be estimated as to the point where the coercive field changes from symmetrical to asymmetrical. If the temperature is higher than the Neel temperature, antiferromagnetic order is disrupted. The Neel temperature for 10% manganese in nickel is estimated at 14 Kelvin.

The hysteresis loops are also noted to shift toward the –x axis. This is known commonly as an exchange bias. As this 'exchange bias' decreases at higher temperatures, the coercivity is enhanced. This is contrary to typical results. [59] It is my belief that this shift is primarily due to nonuniform granular coupling, see Chapter 5 for structure of these samples. Recent studies suggest that the intergranular coupling is stronger than the ferromagnetic / antiferromagnetic exchange bias. This study further indicates grain size is the primary contribution to an exchange bias [60].

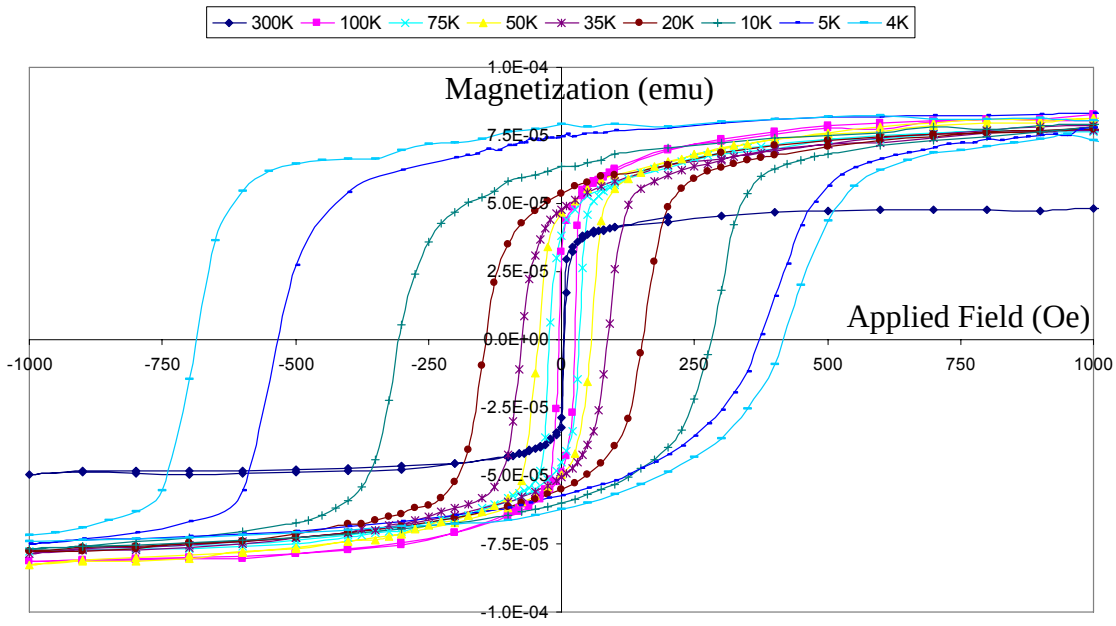

Figure 31: Hysteresis loops taken (Magnetization (emu) vs. applied field (Oe)), showing change in the saturation magnetization and hysteresis of a x=10% concentration manganese in nickel alloy.

Figure 32 is a plot of how the magnetic susceptibility and magnetic energy varies as a function of temperature. The susceptibility is the slope of the measured vs. applied field curve taken at zero applied field. The magnetic energy is defined as the area of the measured vs. applied field hysteresis loop. As the temperature increases we note a sharp decrease in the susceptibility and a sharp increase in the energy. These changes are expected, since it should take more energy for the frozen spins to move with the field. The susceptibility is physically how well the spins respond to the field. As the temperature warms toward 100 Kelvin, the sample's spins responds more readily to an applied field compared to at 100 Kelvin.

4.4. Summary

In conclusion, magnetic dichroism and hysteresis measurements were performed to show the local and nonlocal magnetic effects on manganese doped nickel. Locally, the nickel moment shows strong ferromagnetic behavior with manganese and has great changes with field and concentration of manganese. This shows that nickel has the predominant magnetic control in the sample and mimics bulk behavior for small concentrations of manganese. The nonlocal hysteresis loops show evidence of a spin glass transition at 15% manganese in nickel at 100 Kelvin. Furthermore, an exchange bias is observed as a result of granular coupling in the alloy below 50 Kelvin.

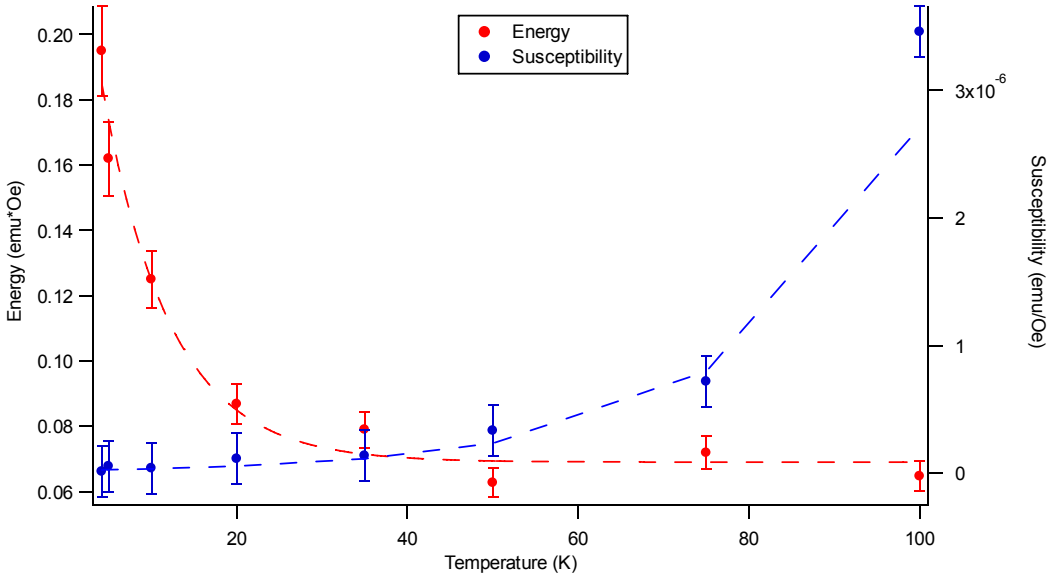

Figure 32: Energy & Susceptibility vs. Temperature for 10% Mn in Ni. We note that the increase in susceptibility and decrease in energy as temperature increases is a result of the moments become unfrozen from a pseudo spin-glass phase.

Chapter 5

Case study of 10% Manganese in Nickel……

5.1. Lattice structure of Nickel Manganese

Nickel grown concurrently with manganese concurrently has different phases and a complex phase diagram depending on how it is grown. Also, silicon substrates have been shown to order into many different structures but for our experiments, the Si(100) 2x1 reconstruction was achieved following a procedure due to Hu et al [22] and shown in figure 33.

Long range ordered alloy structures have been found for $Ni_{75}Mn_{25}$ and $Ni_{50}Mn_{50}$. The half mix of nickel manganese is antiferromagnetically aligned for nearest Mn atoms and ferromagnetic alignment for next nearest atoms [61]. At this point, manganese dominates the magnetism with measurements of nickel moments to be at most 33% of bulk value [62]. Thin films of a wide range of concentrations of nickel manganese has been shown to grow layer by layer and show p(1x1) [63] and c(2x2) [64] surface reconstruction when grown on Cu(100).

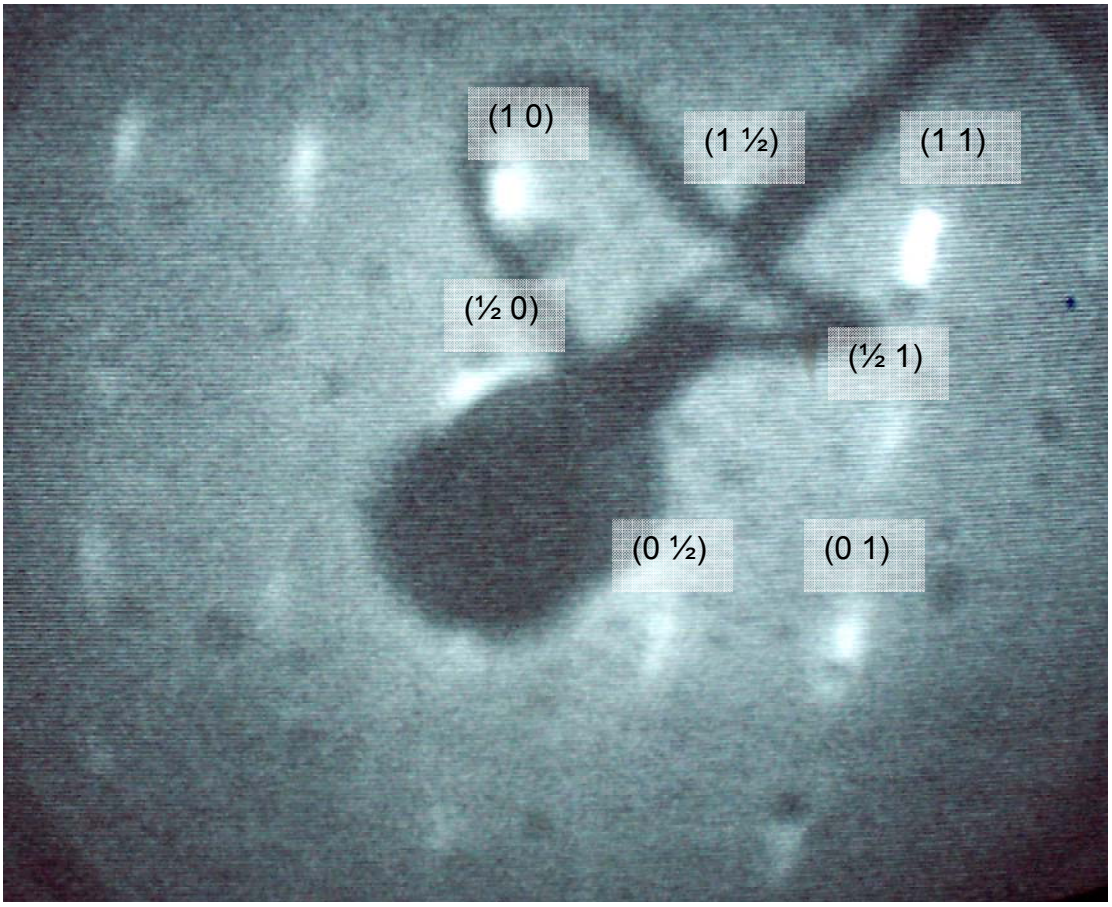

Figure 33: LEED pattern of Si <100> showing a 2x1 pattern.

5.2. Samples Prepared

Samples in chapter four and mostly in chapter five are prepared on a polished silicon (100) wafers. They are composed of Cu 30 Å /$Ni_{1-x}Mn_x$ 100 Å / Cu 20 Å, where x varies based on set evaporation rates. All of the films prepared in this study were grown in a separate preparation chamber at a base pressure of ≈ 5 x 10^{-10} Torr. Electron bombardment from independent evaporators was used at rates no greater than 5 Å per minute. The final copper layer was used as a capping layer to prevent the oxidation of the magnetic alloy's surface.

The growth was performed with the sample at room temperature and the sample was not annealed during the processes, ensuring random substitution of the nickel manganese alloy. Composition was monitored by a quartz crystal microbalance and concentrations were checked from x-ray core level photoemission (XPS) data. Mn segregation to the surface and clustering in the bulk was minimal under these conditions, as reported by Borgatti et al. [65].

5.3. Scanning Electron Microscope Imaging

A microscope is a useful tool to see how uniform a sample has been grown, grain boundaries [66], crystallographic orientations [67], and many other physical phenomena. However, there is a limitation to the magnification/resolution of a conventional microscope. Electrons can be used instead of light in a microscope, known as a Scanning Electron Microscope (SEM). Similarly to traditional microscopes, the SEM uses magnetic lenses to focus the electron beam down to a tiny spot. Scanning coils are used near the

sample to focus the beam to different spots. Secondary electrons are ejected from the sample, detected, and are amplified on an imaging array. For a more detailed description of how the SEM works, see the appendix at the end of this document.

Figure 34 is of a 10% manganese in nickel sample's SEM image at a 45 degree angle. This shows not only the top layer, but a side profile of the nanomagnets as well as the silicon substrate. As material was deposited onto the silicon substrate, the deposition obeys VW growth. The nickel manganese alloy repeats this growth, increasing the size of the island growth. Another study found that if the copper was slightly annealed between 350-390 Kelvin, a smooth epitaxial copper layer on silicon (100) can be achieved with little surface segregation [68]. If the film of copper is not annealed, VW growth that has been discussed occurs.

The result is a stacked structure of nanomagets each separated by a random amount based on where the droplets wet. This column like structure has been verified with a similar growth procedure by atomic force microscopy as shown in figure 35 [69]. Atomic force microscopy uses a cantilever and tip to measure the force between tip and surface. This gives a three dimensional view of a sample, however the sample can be no greater than 1mm x 1mm x 1 μm. In this figure as well as my sample in figure 34, the white stripes and dots represent the nanomagnets that are separated by the dark spaces. The size of the nanomagnets vary but are on the order of ~ 10nm for this slice.

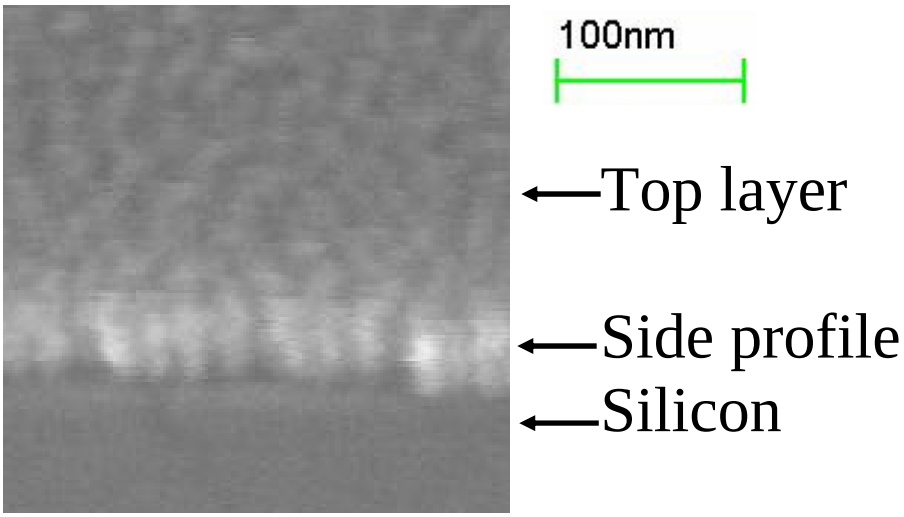

Figure 34: Scanning Electron Microscope (SEM) image scanned at a 45 degree angle showing the silicon substrate, the side profile of the magnetic material (nanomangetic island structure) and the top layer.

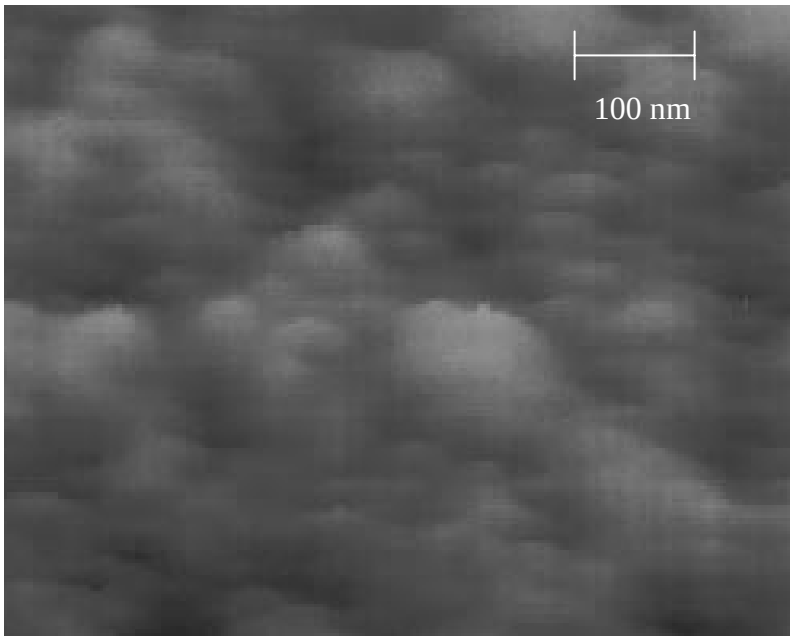

Figure 35: Atomic force microscopy image of nickel deposited on copper (100). The white, cloud-like, image represents the nickel nanomagnets grown that are similar to our samples.

5.4. AC Susceptibility

Frequency dependent AC Susceptibility is a technique to see how fast the spins can respond to a changing magnetic field. AC susceptibility measurements are made using a Physical Properties Measurement System (PPMS). When measuring AC susceptibility (ACMS), the sample remains fixed while a small AC field is used along with a constant DC field. This method is popular in measuring small signals through lock-in techniques [70]. The induced AC moment (M_{AC}) is:

$$M_{AC} = H_{AC} \sin(\omega t) \, (dM/dH) \qquad (21)$$

where H_{AC} is the AC applied field, ω is the angular frequency of the applied field, and dM/dH is the susceptibility of the sample.

Consider a cylindrical rod alternating in a magnetic field. According to Landau and Lifshitz [71], the magnetic field can be broken up into a static dc component, B_{dc}, and a variable ac component, B_{ac}, equation 22:

$$B = B_{dc} + B_{ac} = B_{dc} + B_a \cos(\omega t) \qquad (22)$$

The susceptibility can change as the spin dynamics of the sample changes. This magnetization is directly proportional to the applied field as shown in equation 22. Therefore one can write the complex suscebilties as [72]:

$$\chi' = \frac{1}{\pi B_a} \int_0^{2\pi} M(\omega t)\cos(\omega t) d(\omega t) \tag{23}$$

$$\chi'' = \frac{1}{\pi B_a} \int_0^{2\pi} M(\omega t)\sin(\omega t) d(\omega t) \tag{24}$$

where χ' represents the real part of the susceptibility while χ" represents the imaginary part. The imaginary part of the susceptibility represents the energy converted into heat during a cycle while the real part represents the magnetic energy stored in the sample [73].

As the frequency ω is increased from zero (DC case) to higher frequencies, the spins are less likely to respond to the applied field. The samples magnetization lags behind the driving field. The susceptibility therefore can be split into two parts: a real part (the DC susceptibility), and the imaginary part (the time lag of the spins). Figure 36 is the case of 1% of manganese added into copper. The AC susceptibility is a measured of this spin glass [37].

Figure 35 shows a freezing temperature, T_f, that occurs at a transition in the imaginary component of the susceptibility. As the temperature cools from 300K to near the freezing temperature, the imaginary component of the susceptibility increases. This increase in the imaginary susceptibility, or lag in the magnetic spins, is expected. Below the freezing temperature the lag then suddenly decreases as the spins freeze into fixed spin states.

We have made similar AC susceptibility measurements for a 10% manganese in nickel sample performed by SQUID as shown in figure 37. We note a similar behavior to that in figure 36, but occurring at a much higher

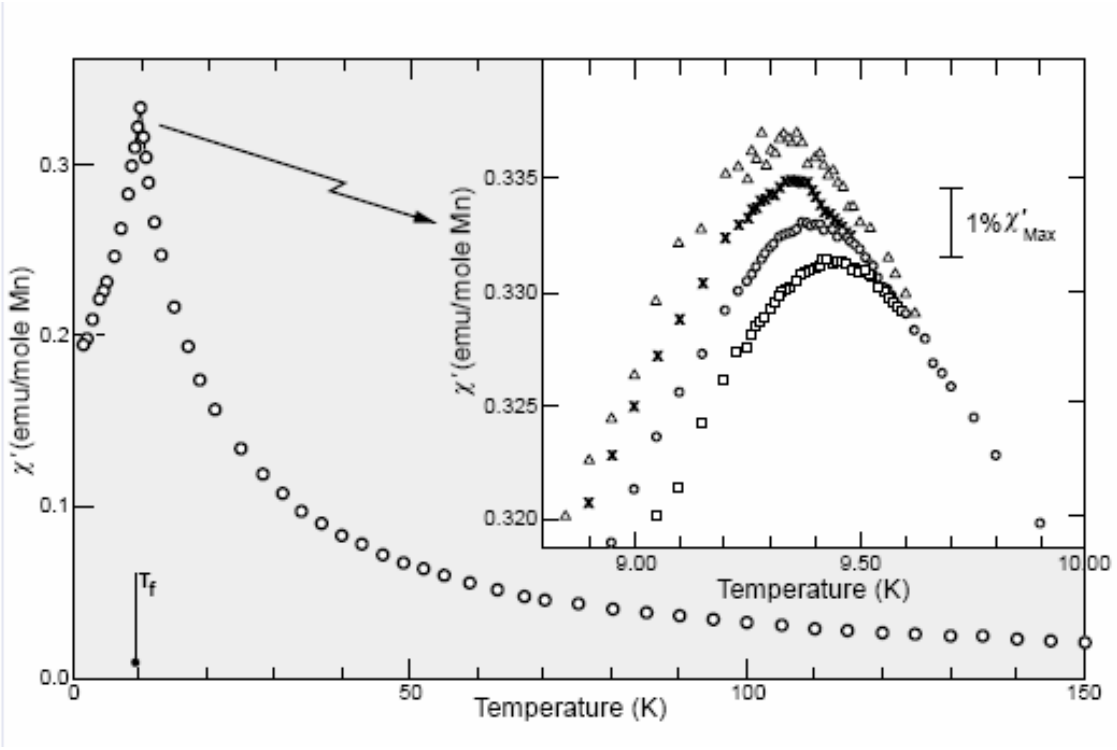

Figure 36: AC Susceptibility measurements for $Cu_{99}Mn_1$ (reproduced from [37]). The peak in the imaginary part of the susceptibility is marked as the freezing temperature. A frequency dependent change occurs at the freezing temperature, as shown in the inset does not occur at a cusp and is rounded instead.

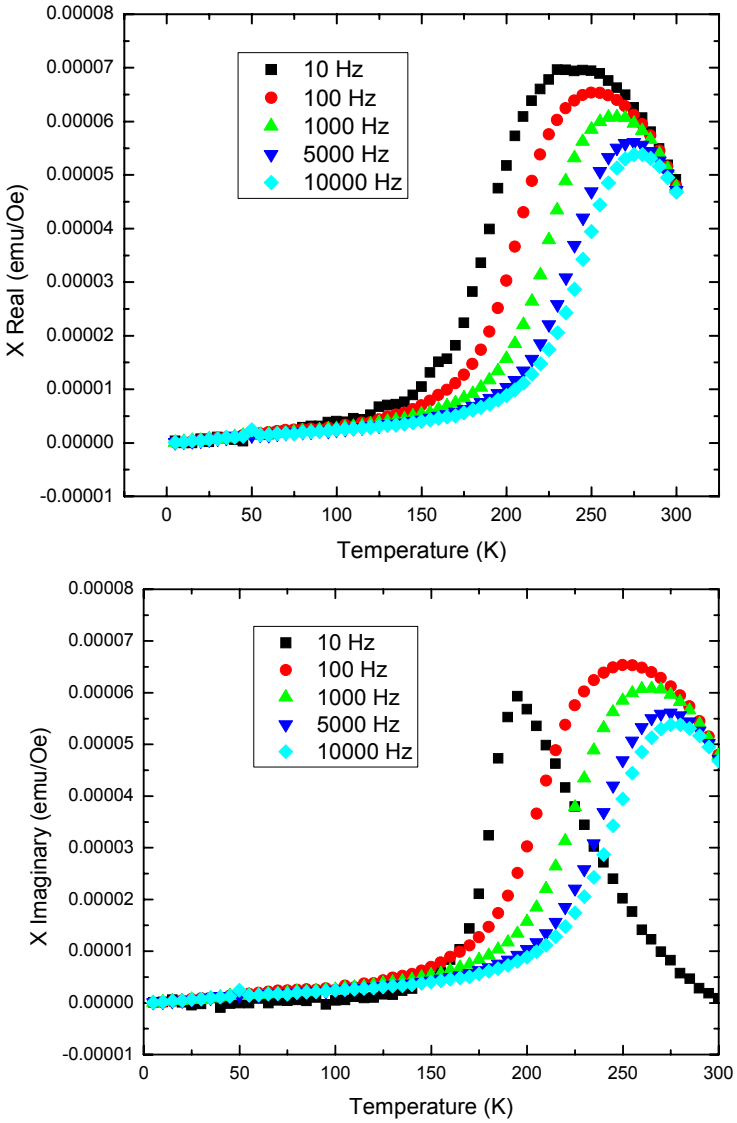

Figure 37: AC susceptibility measurements for 10% manganese in nickel. The peak in the real and imaginary parts of the susceptibility decreases in temperature as the frequency decreases.

‘freezing temperature.’ This is due to the enhanced drag on the manganese moments in a ‘viscous sea’ of itinerant nickel spins.

AC susceptibility behavior in nickel manganese is similar to blocking of single domain particles in rock formations [74]. Magnetic particles in rocks are small enough to contain a single domain, yet are large enough to carry a net magnetic moment. Having a magnetic moment while being thermally influenced, i.e. paramagnetic interactions, is called superparamagnetism. The rocks get their large moment from anisotropy due to shape, crystalline structure, or possibly external stress. The susceptibility of these rocks is proportional to the distribution of blocking temperatures. A cluster of spins only contributes to the susceptibility if the temperature is greater than the blocking temperature for that cluster. These are the yet to be frozen clusters.

Our nickel manganese system starts out in a paramagnetic state with pockets of ferromagnetism when examining temperatures above the turning point of the curve. This is due to clustering of spins or creation of small nanomagnets that have thermal energy stronger than magnetic coupling forces in their proximity. An effective Curie temperature can be achieved where the system gradually shifts into becoming a weak ferromagnet. A plot of the inverse susceptibility versus temperature is created in figure 38. By extrapolating the slope to zero inverse susceptibility, an effective Curie temperature is measured to be 183 Kelvin.

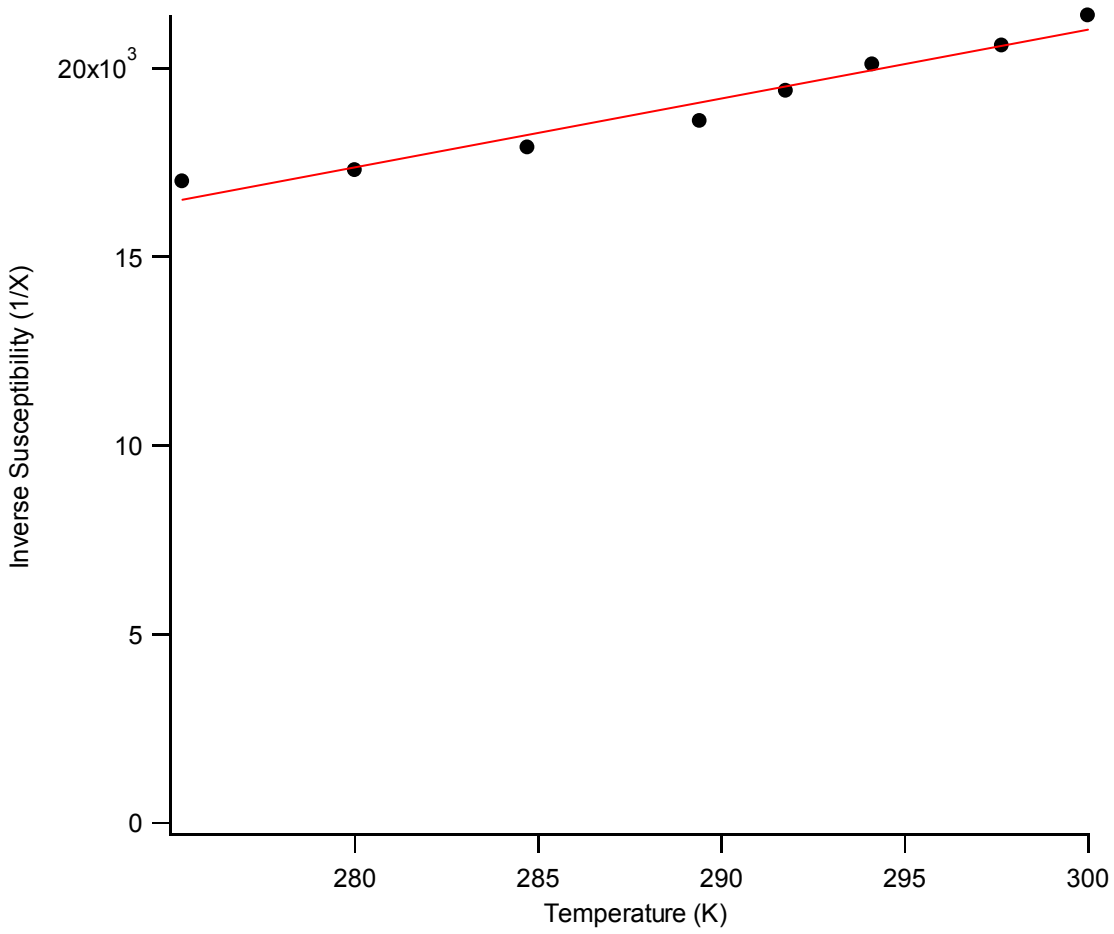

Figure 38: Inverse susceptibility versus temperature plotted for 10% manganese in nickel. A best fit line is shown to determine the location where the inverse susceptibility goes to zero to determine the effective Curie temperature.

A shift in the peak position to higher temperatures as the frequency increases also correlates to a blocking. If there were no change in the peak position, a sharp magnetic phase transition could be a possibility. We note that a shift of 50 Kelvin from frequencies of 10 Hz to 10 kHz. This small shift over a large frequency range indicates the activation energy for thermal processes is very large. This energy is estimated from a Neel blocking model [75], in which the relaxation time of a single domain cluster is given as:

$$\tau = \tau_o e^{E_a / kT_B} \tag{25}$$

Where T is the relaxation time and E_o is the thermal activation energy. We interpret from our data that the activation energy is 1.2 eV. This energy is much higher than other spin-glasses [76] [77], however this higher energy is attributed to the extra energy created by having a sea of itinerant ferromagnets, namely nickel.

The broad characteristic of the curve corresponds to a wide distribution of clustering size, namely different size nanomagnets. At the peak blocking temperature, the larger clusters are blocked together, while the smaller clusters break away at lower temperatures. [78] This occurs until magnetic moments begin to freeze into a final spin glass state.

5.5. Field Cooled vs. Zero Field Cooled Measurements

Another method to observe the spin dynamics of a sample is to measure the magnetization of the sample with two different applied field scenarios. In the field cooled measurements (FC), the sample is simply cooled in an applied field nd AC field measurements are made using the SQUID. Measurements are also made using the SQUID for zero field cooled (ZFC) measurements, using a different procedure for cooling. First, the sample is demagnetized, then the sample is cooled. Next a field is applied, the measurement takes place, and this cycle is repeated. This way there is no field present during the cooling process. The difference between these two measurements is a signature of spin glass behavior. The spin-glass phase of $Ni_{1-x}Mn_x$, x = 22%, has also been studied extensively [79] [80]. However studying emergent spin glass behavior for lesser concentrations of manganese in nickel has not been explored to date. Figure 36 are the first of such measurements.

Oner et al. has looked at $Ni_{76}Mn_{24}$ and measured the FC and ZFC case, as shown in figure 39 [81]. The T_C of the sample is where the magnetization goes to zero temperature around room temperature. There is an immediate divergence in the magnetization cooling from room temperature down. The two curves match up well between 100 and 150K followed by another divergence below 100K. A divergence in the ZFC and FC is a signature of a spin glass state or a freezing of the magnetic spin moments. This alloy shows such a divergence at nearly all temperatures, signifying a broad transition into the spin glass state.

My 10% manganese in nickel sample is measured using ZFC and FC measurements. The applied magnetic field used is 1 Tesla. To zero out the

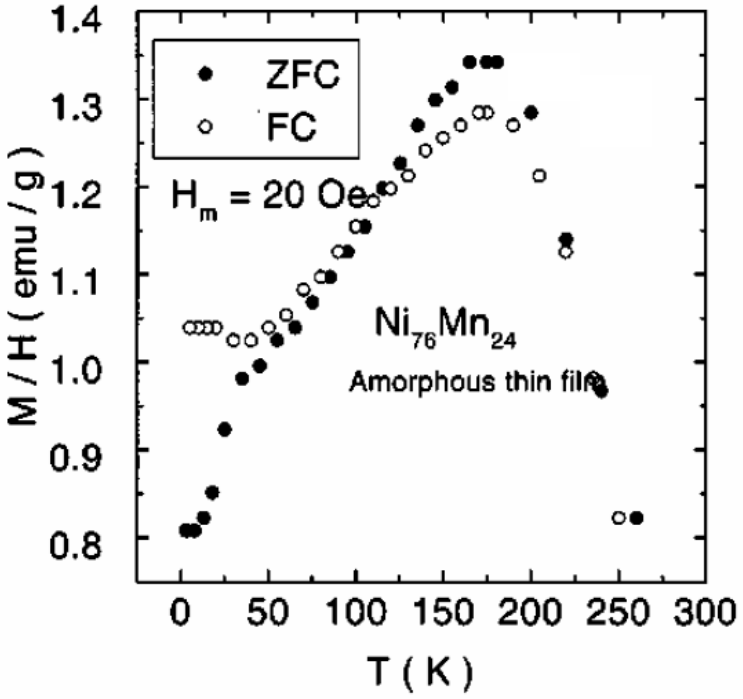

Figure 39: Field cooled (o) and zero field cooled (o) measurements shown with magnetization versus temperature for a $Ni_{76}Mn_{24}$ sample (as reproduced from [81]). The divergence between the two scans begins near room temperature and diverges again around 100 K.

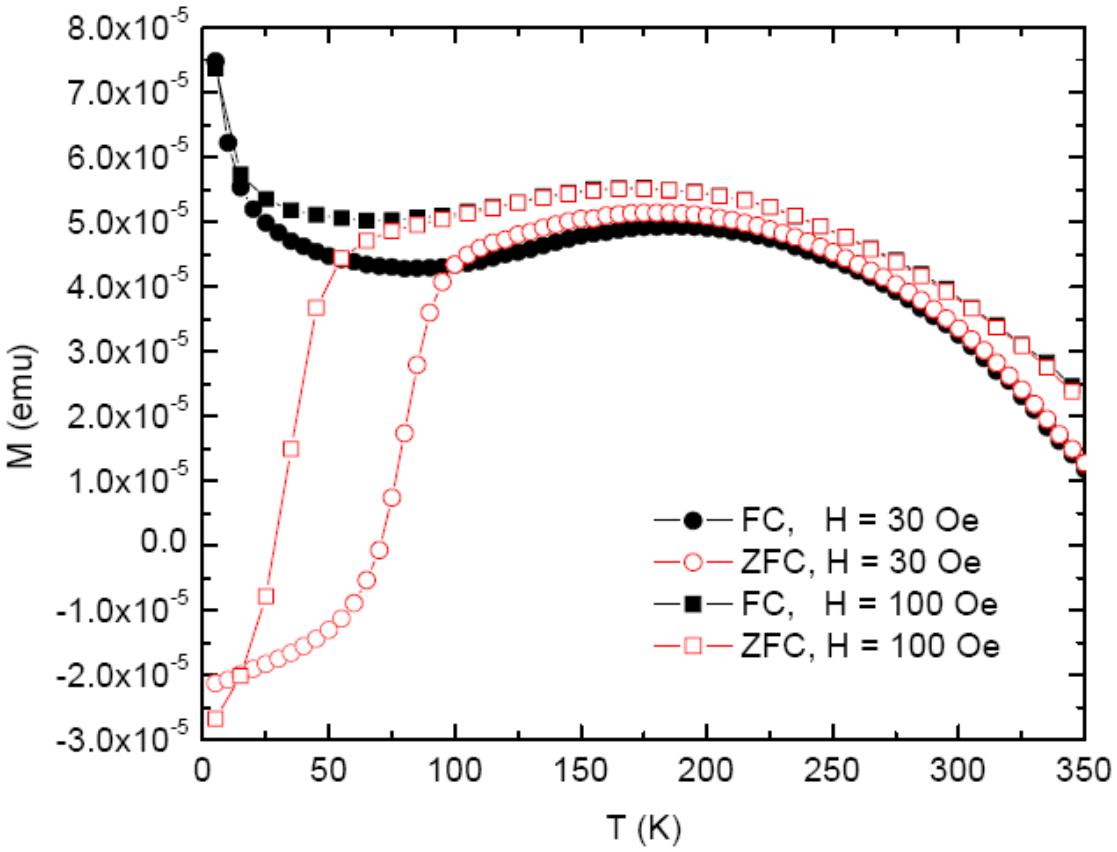

Figure 40: Field cooled and zero-field cooled measurements for 10% Mn in Ni. We note the bifurcation at 100 Kelvin for both applied magnetic fields.

magnetic field, since there is a remnant magnetization in the sample, a small field is oscillated to zero in the sample. Figure 40 shows the results for measuring this sample at 30 Oe and 100 Oe. The Curie temperature can be estimated at higher temperatures and decreasing in amplitude. Having the real peak at lower, dc-like frequencies, because this is the most energetic the sample can be and would involve the least switching of spins with frequency. As the frequency increases, magnetic spins will have a tendency to flip more, causing the peak in the susceptibility to decrease. More heat is converted into energy at the lower frequencies due to the greater required energy to flip the magnetic spins.

The Curie temperature is a temperature where the material loses ferromagnetic behavior and becomes paramagnetic. When the magnetization versus temperature curve goes to zero, the sample becomes nonmagnetic unless an external field is applied. From these plots, since the Curie temperature should be where the curve goes to zero at the higher temperatures on the right hand side of the plot. I estimate the Curie temperature is between 375 K and 400 K, which is close to a predicted value of 405 K [9].

Also noted is a bifurcation in the field cooled and zero field cooled runs. This bifurcation occurs around 100 K. This shows that if the sample is cooled below 100 K, it enters a spin glass state where the field cooled measurements are a representation of the frozen magnetic spins. By measuring in zero field cooled mode, the sample is allowed to demagnetize at lower temperatures. These are all signs that the material has began a reentrant spin glass (RSG) phase for these nanomagnets [80]. At high temperatures, RSG's start out with

ferromagnetic alignment, yet exhibit anomalous magnetic behavior at lower temperatures that are characteristic of spin glasses. The theoretical transitions between phases using a mean field model have been theoretically analyzed [82] and later enhanced [83].

This phase has also been studied for another weak itinerant ferromagnet, FeN deposited on Si(100), and exhibits similar behavior [84]. At a critical temperature of 120 Kelvin and below, the sample becomes difficult to be magnetized and needs a much larger field to be saturated (50 kOe). However, the trend of field cooled and zero field cooled measurements matches well with our data.

The enhanced magnetism observed at temperatures less than 25 Kelvin has gained recent interest. This upturn maybe be due to Bose-Einstein condensation where magnons coalesce and increase the magnetism at these temperatures [85]. This result is consistent with previous findings of nanomagnets using cobalt-platinum alloy and a nickel-copper alloy [86]. Further understanding of materials such as nickel manganese and other weak ferromagnets can improve performance in the many devices that use magnetism.

5.6. Hysteresis with Copper (100) Substrate

In order to check to see if morphology plays a key role in the sample preparation, a sample was grown on Cu(100), a different substrate entirely compared with Si(100). This substrate was polished with diamond pastes mixed with a few drops of machine oil on top of nylon disks. Each paste started with the

largest bead size and worked its way down. The motion of polishing was rotated by 90 degrees between each paste. This way, I knew when one stage of polishing was done by not being able to view the scratch marks in that preferential direction. After each state, the crystal was washed in deionized water and new sample preparation gloves and nylon disks were used to prevent cross contamination between stages of polishing.

The copper crystal was then mounted into the preparation chamber. Succesive annealings and argon bombardment was used until the sample had RHEED spots appear on the screen. Then a sample was made with the evaporators with thicknesses of 30nm of $Ni_{90}Mn_{10}$ followed by 5nm of copper to prevent oxidation of the nickel manganese.

The sample was scanned using SQUID to determine hysteresis effects at various temperatures. The results are shown in figure 41. The saturation magnetization remains relatively constant with temperature while the coercive field shrinks a little, but not nearly as great as the nanomagnet's coercive field.

Comparing hysteresis data on Cu(100) to the samples grown on Si(100), the coercive field shrinks less and there is no exchange bias. The small difference in the coercive field is likely from a gain in magnetic spin energy between the ferromagnetic nickel and antiferromagnetic manganese. It has been verified that this small change in coercive field is due to exchange coupling between nickel layers [87]. In the nanomagnetic sample, the change is due to not only the exchange coupling between nickel but also primarily due to

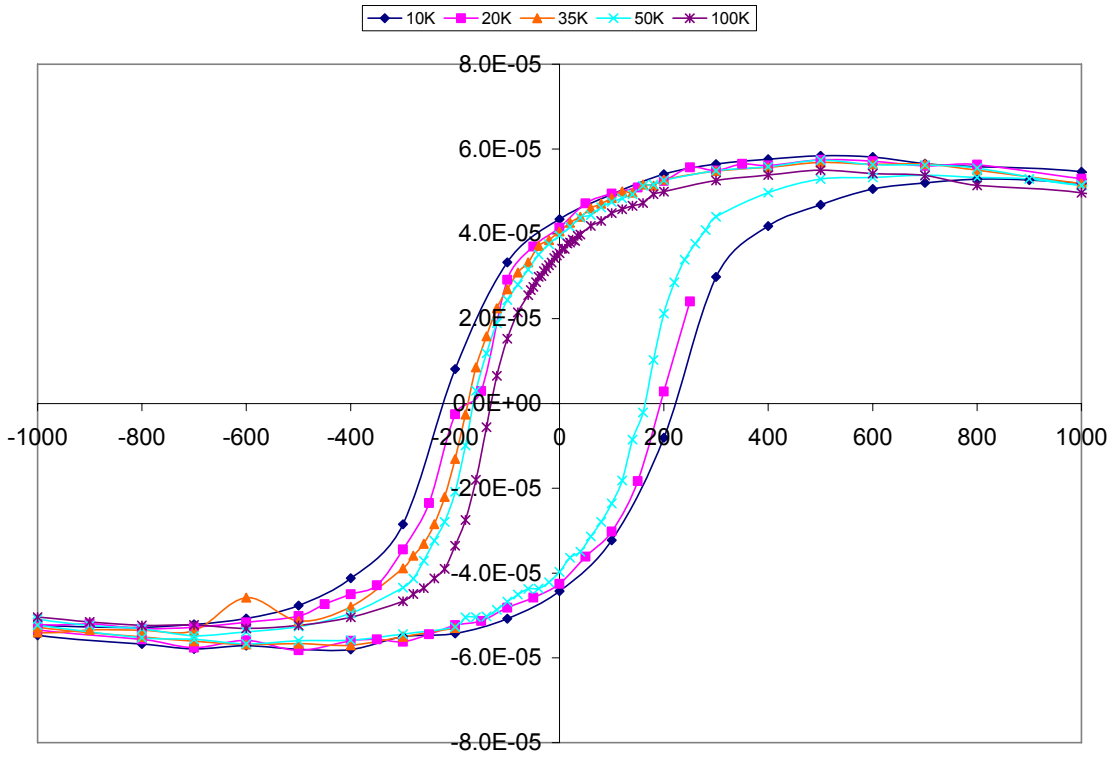

Figure 41: Normalized magnetization vs. magnetic field (Oe) hysteresis loops measured by SQUID at various temperatures of $Ni_{90}Mn_{10}$ grown on Cu(100). Less spectacular changes occur in the hysteresis compared to the nanomagnets grown on Si(100).

coupling between nanomagnets [87]. Most of the previous measurements were done at 100 Kelvin where there is no exchange bias, therefore these results are not expected to be different because of these effects. Only at temperatures lower than 50 Kelvin would we have to account for this exchange.

Chapter 6

Conclusions & Future Directions……

6.1 Conclusions

Since the birth of spintronics research, many in the community have put forth great effort to better understand transitions between ferromagnetic and antiferromagnetic interactions. Nickel manganese is a prime example due to its increasing ferromagnetism up to 8% followed by decreasing ferromagnetism beyond 10% concentration, and spin glass behavior above 20%.

By growing and studying this alloy, many unique features were observed. By diffusing manganese into a host nickel substrate, the sp bands were studied where they cross the Fermi energy. Previous work showed that the dopant would either decrease the minority peak for antiferromagnetic interactions like chromium or change the location in momentum space like iron. Maganese dopants however decreased the spin majority peak while increasing the spin minority peak. Furthermore, there was no shift in momentum space, suggesting very little change in the exchange energy between nickel and manganese atoms.

Measurements for the nonlocal and local effects of nickel manganese were also explored. The nonlocal magnetism was investigated using SQUID and

measuring hysteresis loops. At 15% of manganese in nickel the saturation magnetization and coercivity drops to near zero. This separates the magnetic properties into two parts. When the manganese concentration was less than 15%, mostly ferromagnetic interactions occurred. Above 15%, the samples transitioned into a reentrant spin glass where the moments would be frozen in different magnetic orientations. The samples also showed an exchange bias dependent on nanomagnetic structure.

These samples were also measured using magnetic dichroism to investigate the local magnetic effects. The magnetic dichroism measurements show similar features to the hysteresis loops. By examining only the nickel atoms, we see the enhanced moment at 5% followed by the drop to zero magnetism at 15% and the rise into the precursor spin glass state. We also note ferromagnetic coupling from similar lineshapes for the nickel and manganese as expected.

Lastly, a case study on 10% of manganese in nickel was considered. AC susceptibility measurements were performed to explore timing effects on changing magnetic spins. It was found that an effective freezing temperature around 200K was measured, much higher than typical spin glasses because of the stronger coupling due to the sea of itinerant ferromagnetic spins. Field cooled and zero field cooled measurements were performed to further investigate this spin glass property. These measurements showed the sample's T_C to be around 400K which matches theory and shows a bifurcation in the measurements around 100K. The curves match most closely with nanoisland pictures such as

those from iron nitride nanoparticles. SEM pictures verified that these are indeed nanoislands, and that when cooled below 50 Kelvin, the nanoislands experience an exchange bias primarily due to coupling amongst these islands.

6.2 Future Directions

Many previous discoveries and techniques can still be used to get further insight into this unique alloy. Inverse photoemission could be used to study the unoccupied electronic states in solids and in surfaces for this nickel manganese alloy [88]. This way we would be able to examine not only the occupied levels below the Fermi energy, but also the levels above the Fermi energy. Experiments have already been performed on $Ag_{95}Mn_5$ that showed the virtual bound state of Mn [89]. Repeating these experiments with manganese in nickel can help identify how manganese changes the magnetism in nickel through band filling.

Through examining the LEED patterns, Kirschner was able to examine the interlayer spacing , or how well the alloy fits on top of the substrate [64]. Figure 42a shows RHEED oscillations characteristic of layer-by-layer growth of nickel manganese on copper. Figure 42b shows how the interlayer spacing varies versus the percent nickel. Note that below 50 percent nickel, the lattice mismatch is too great to get an ordered structure from LEED and the RHEED oscillations become nonuniform. We are not overly concerned with this since the alloy is nonmagnetic in this region. Other than this, the alloy deposits well in ordered structures for all other concentrations of concern to use.

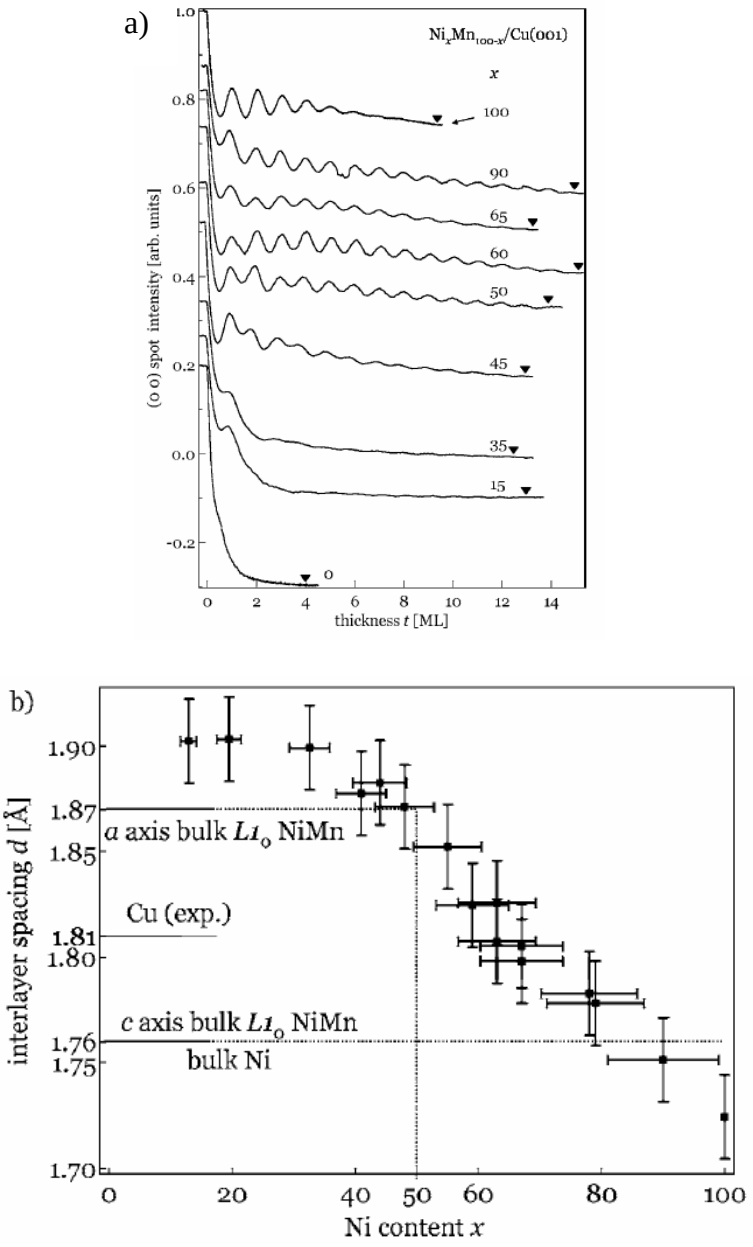

Figure 42: (a) RHEED oscillations on nickel manganese alloys performed by Kirchner [64]. This shows the layer by layer growth that can be achieved on copper at an concentration of manganese in nickel. (b) Spacing between the atoms on the top layer vs. the concentration of nickel in the NiMn alloy. Noted is the repeated structure at 50% and the well fit.

Magnetic anistotropic properties were measured by hysteresis loops using Magneto-Optical Kerr Effect (MOKE). Anistropy is the difference in magnetic properties of a sample by changing various quantities such as thickness of the sample or orientation of the crystal. Schumann et al. [63] looked at how the various anisotropies affects the spin reorientation magnetization of samples with different thicknesses. The effective or net anisotropy looked at were the volume, K_v, surface, K_s, and shape anisotropy, $2\pi M^2$. This can be written as:

$$K_{eff} = \frac{2}{d} K_s + K_V - 2\pi M^2 \qquad (26)$$

The results of these experiments are plotted in figure 43a. For small concentrations of manganese in nickel (less than 8%), the transition from in plane to out of plane magnetization is relatively constant. After 8%, the magnetization of the sample starts to decrease and Schumann's data suggests that the transition to out of plane magnetization happens at thicker films. These thicker films have a greater volume anisotropy. Therefore the films can grow much thicker until the magnetization switches out of plane.

The saturation magnetic field vs. inverse thickness for 13% manganese in nickel is plotted in figure 43b. The linear trend that follows is expected since the relation in equation 26 is linear for H_s vs. d^{-1}. It would be interesting to follow this up and try layered structures such as cobalt with nickel manganese and see if this same relation can be used.

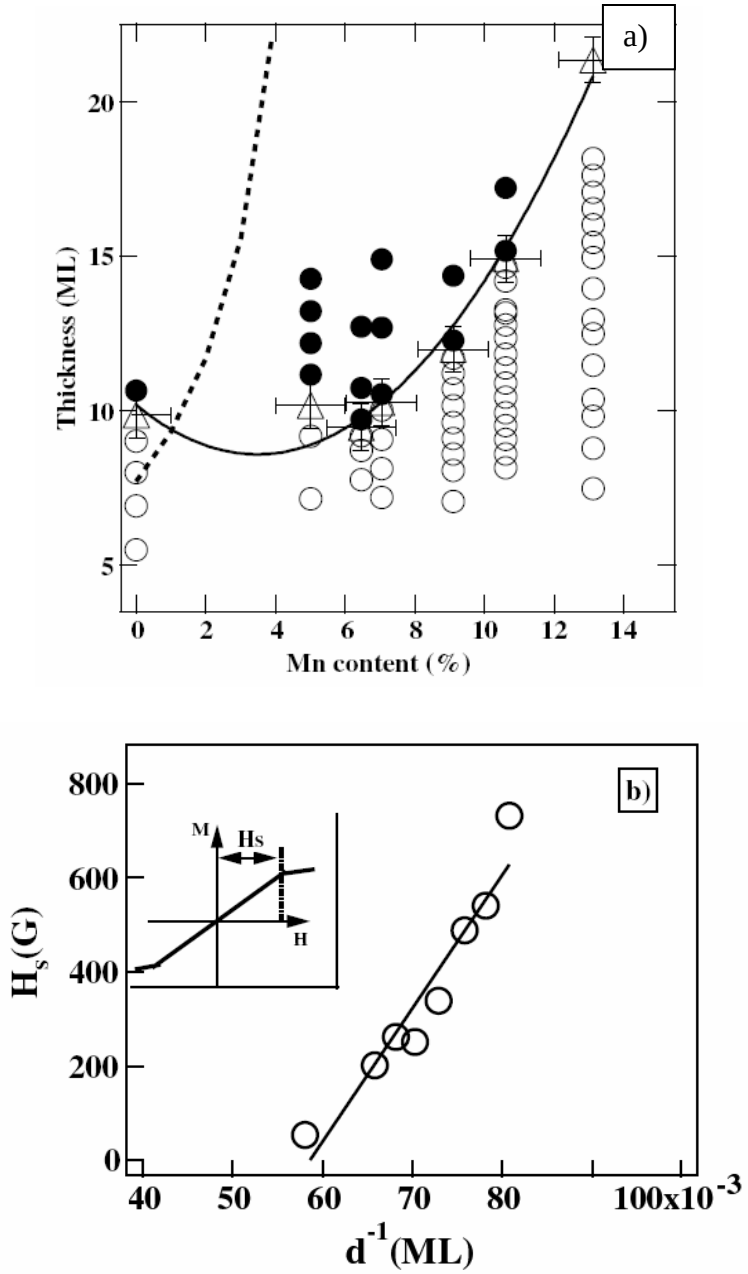

Figure 43: (a) The orientation of M (in-plane o, out of plane ●) as a function of concentration and thickness at 300K is shown. (b) The saturation field (H_s) versus the inverse thickness of $Ni_{87}Mn_{13}$. A linear trendline is fit through the data.

Another idea would be to create multilayers with this nickel manganese alloy. This could provide key insights as to the physics behind this material. Kirschner looked at cobalt deposited as a buffer layer either directly on copper or on top of the nickel manganese film [64]. He found that by depositing cobalt on copper before the nickel manganese alloy, little changes with the hysteresis loops. However a great change in coercivity is measured by depositing the nickel manganese alloy directly on copper and then depositing cobalt on top. Furthermore, an exchange bias is noted for the Co/NiMn/Cu(100) system even though the system was not field cooled. This small exchange bias is explained as a small temperature effect when depositing on the sample. Whether it is finding a material that increases scattering but does not decrease transmission current for use in GMR devices or to understand the physical nature of what makes the magnetic material spin flip, multilayers can provide this further insight.

Also, creating a wedge sample cell where the composition of the sample continually varies would provide quicker experimental insight. [90] [91] This could be accomplished in vacuum by using a pneumatic shutter that would block the evaporation in stages. The sample would start growing layer-by-layer, then through the use of the shutter, more thickness would appear on one side of the sample than the other. This way, an entire experiment based on the thickness of a sample can be performed with one sample. Compositions of different alloys could also be varied to provide only one sample for all measurements. This way there would be no questions as to different growth conditions from different samples.

Another future experiment would be to plot a phase diagram of nickel manganese similarly to Coles [92] and Childress [93]. The key difference in their phase diagrams is that they looked at AuFe and CuCo which are paramagnetic if there are high enough concentrations of Au or Cu. In NiMn system, there are mostly ferromagnetic and spin glass states. Ogawa et al. did such a diagram for 22% manganese in nickel, shown in figure 44 [80]. The spin glass state for these films occurred at temperatures of 45 K or lower depending on thickness. These films were uniform layer by layer, hence the lower temperature for transition. Other key features of the graph are the transition from paramagnetic (PM) to spin glass (SG), as well as the critical thicknesses D for the Curie temperature D_C and spin glass D_{FM}^0. The temperatures were determined from susceptibility measurements versus temperature where the field cooled and zero field cooled measurements diverge (T_{RSG}) and where there is an inflection in the susceptibility measurement (T_C).

By plotting out this transition from ferromagnetism to spin glasses not only would we gain insight as to at what temperatures these transitions occur for different alloys, but also new phases may appear which have not yet been fully explored.

There are many future insights that can be discovered in this vast field. By understanding how magnetism operates, both industry and sciences can be furthered in a profound way.

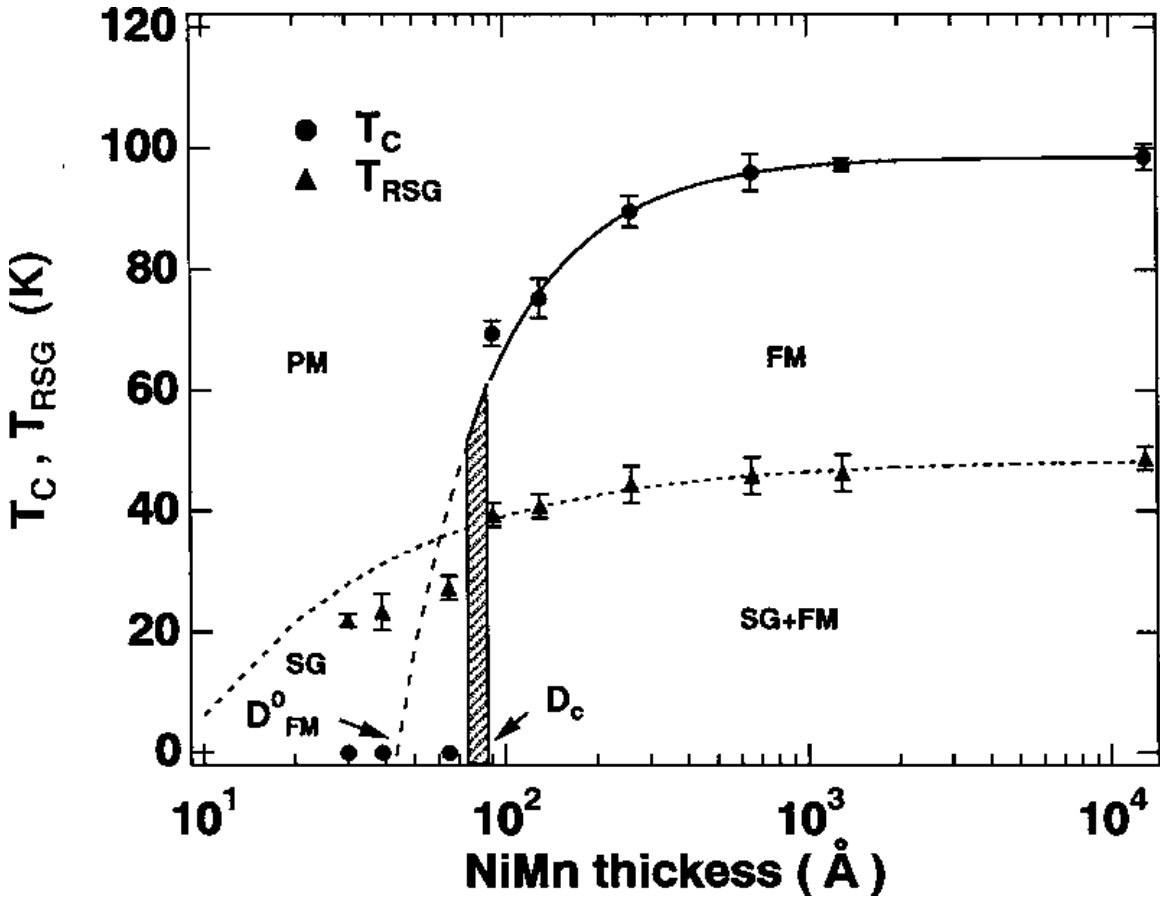

Figure 44: Temperature and thickness dependence of a 22% manganese in nickel sample grown on copper. The spin glass state occurs at 45 K for thick films and decreases for thinner films. [80]

Appendix……..……

Scanning Electron Microscope (SEM)

A.1. Electron Gun

The electron beam in a scanning electron microscope comes from a hot filament, typically made of tungsten. This gun is typically encapsulated both thermally and electrically. Outside this cap are plates with a gap. Each plate is held at a positive potential with respect to the filament. This forms a strong electric field that has the electrons strongly attracted to the area near the plates. This is similar to molecular beam epitaxy (MBE) discussed earlier in chapter two. Some of the electrons strike the plates while others pass through them. It is these electrons that pass through that are used for the SEM. This differs from MBE where the goal is to have as many electrons strike and heat up the plate.

A.2. Lens and Scanning Coils

After the electron gun, the electrons follow many different lenses. A cylindrical magnetic creates a spiraling effect for the electrons by applying a magnetic field in the longitudinal and radial direction. Other lenses such as a

condenser lens follow to reduce the electron beam to a very fine point. Spot size is crucial for the resolution of the instrument. The smaller the spot size will produce a higher resolution for a scan. The spot size for a typical SEM is 10nm, although 1nm spot sizes or less can be achieved with some skill [94].

To change the location of the beam or penetration energy, scanning coils are used. These coils have an applied magnetic field to pull the electrons to each individual location on the sample. An entire schematic is shown in figure 45.

A.3. Sample

The sample must be placed in vacuum of at least 1 x 10^{-5} Torr. Gases in atmosphere could react with the electron beam or hinder the transmission of the electron beam. This would reduce the contrast of the instrument.

Lastly, the electrons hit the sample producing secondary electrons. These secondary electrons are collected by a secondary detector, converted to voltages, and amplified. The amplified voltage is applied to a grid and causes the intensity of a point to change. The image consists of thousands of these points that correspond to the topography of the sample.[95] Magnification can range from 15 to 100,000 times the size or more.

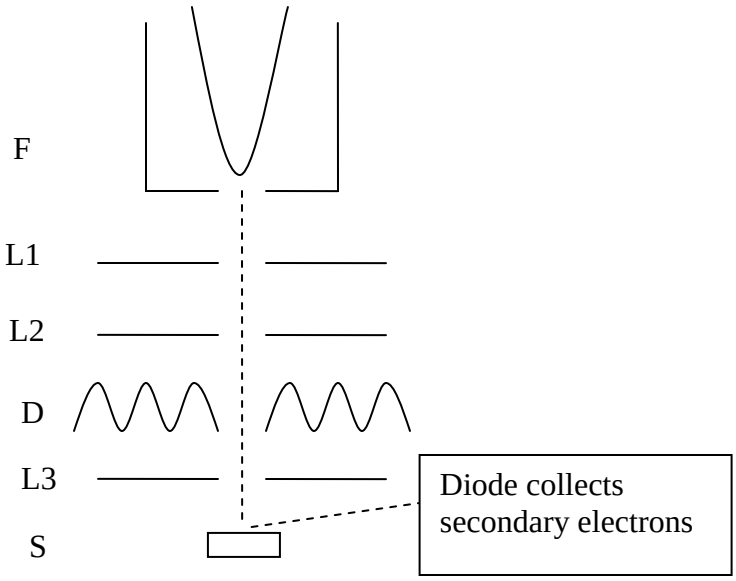

Figure 45: Schematic showing the basic principle for a scanning electron microscope (SEM). The filament (F) is shown in an insulating case. Three lenses are shown (L) that are used to focus the beam. Scanning coils (D) are used to move the beam to different locations on the sample (S).

References

[1] M. R. Cohen and I. E. Drabkin, *A Source Book in Greek Science* (Harvard University Press, Cambridge, 1966).

[2] J. Needham, *Science and Civilization in China* (Cambridge University Press, Cambridge, 1972).

[3] S. Sambursky, *Physical thought: from presocratics to the quantum physicist* (Pica Press, New York, 1974).

[4] L. P. Williams, Isis **74**, 492 (1983).

[5] Friedrich, Bretislav, Herschbach, and Dudley, Physics Today **56**, 53 (2003).

[6] R. M. Bozorth, Physical Review **79**, 887 (1950).

[7] K. Huang, *Statistical Mechanics*, New York, 1987).

[8] T. Kaneyoshi, J. Phys. F. **5**, 1014 (1975).

[9] Landolt-Börnstein, *Group III condensed matter*

(Springer-Verlag

Berlin, 1997

).

[10] S. Gunan and B. J. Nelson, J. Magn. Magn. Mater. **292**, 49 (2005).

[11] S. Y. Hsu, A. Barthélémy, P. Holody, R. Loloee, P. A. Schroeder, and A. Fert, Phys. Rev. Lett. **78**, 2652 (1997).

[12] M. F. Toney, M. G. Samant, T. Lin, and D. Mauri, Applied Physics Letters **81**, 4565 (2002).

[13] Y. H. Yang, C. H. Lai, C. R. Chang, J. S. Yang, and C. K. Lo, J. Applied Physics **89**, 6603 (2001).

[14] R. G. Musket, W. McLean, C. A. Colmenares, D. M. Makow, and W. J. Siekhaus, Applications of Surface Science **10**, 143 (1982).

[15] A. Pimpinelli, *Physics of Crystal Growth* (Cambridge University Press, Cambridge, 1998).

[16] E. Bauer, Zeitschrift für Kristallographie **110**, 372 (1958).

[17] J. Hampton, J. Martinez-Albertos, and H. D. Abruna, Review of Scientific Instruments **73**, 3018 (2002).

[18] A. Stephen, F. Rossi, L. Nasi, C. Ferrari, N. Ponpandian, M. V. Ananth, and V. Ravichandran, Journal of Applied Physics **103**, 053511 (2008).

[19] D. Ouellette, K. Podolak, and R. Willis, University of Minnesota, 2007).

[20] S. Paunovic, *Fundamentals of Electrodeposition* (Wiley, NJ, 2006).

[21] P. Schlesinger, *Modern Electroplating* (Wiley, NJ, 2006).

[22] X. Hu, C. A. Peterson, D. Sarid, Z. Yu, J. Wang, D. S. Marshall, R. Droopad, J. A. Hallmark, and W. J. Ooms, Surface Science **426**, 69 (1999).

[23] K. Heinz, Rep. Prog. Phys. **58**, 637 (1995).

[24] K. Ploog, Angewandte Chemie - Int. English ed. **27**, 593 (1988).

[25] B. D. Josephson, Phys. Lett. **1**, 251 (1962).

[26] R. C. Jaklevic, J. Lambe, A. H. Silver, and J. E. Mercereau, Phys. Rev. Lett. **12**, 159 (1964).

[27] A. E. Berkowitz and K. Takano, Journal of Magnetism and Magnetic Materials **200**, 552 (1999).

[28] K. A. Kilian and R. H. Victora, IEEE Trans. Mag. **38**, 4 (2002).

[29] W. L. O'Brien, R. W. C. Hansen, and B. P. Tonner, Phys Rev A **347**, 148 (1994).

[30] W. W. W. Wagner G. Schutz, P. Kienle, R. Zeller. R. Frahm, and G. Materlik, Phys Rev Lett **58**, 757 (1987).

[31] W. Wagner, G. Schutz, W. Wilhelm, P. Kienle, R. Zeller, R. Frahm, and G. Materlik, Phys Rev Lett **58**, 757 (1987).

[32] B. P. T. G. R. Harp W. L. O'Brien, and S. S. P. Parkin, J. Appl. Phys. **76**, 6462 (1994).

[33] N. A. R. Janke-Gilman, in *Physics* (The Pennsylvania State University, University Park, 2002), Vol. Ph.D., p. 136.

[34] Doniach and Sunjic, J. Phys. C **4**, 285 (1970).

[35] G. Toulouse, Commun. Phys. **2**, 115 (1977).

[36] J. Atwood, Nature Materials **1**, 91 (2002).

[37] C. A. M. Mulder, A. J. v. Duyneveldt, and J. A. Mydosh, Phys. Rev. B **23**, 1384 (1981).

[38] F. J. Himpsel, J. E. Ortega, G. J. Mankey, and R. F. Willis, Advances in Physics **47**, 511 (1998).

[39] RoyalSwedishAcademyofSciences, (http://nobelprize.org/nobel_prizes/physics/laureates/2007/press.html, 2007).

[40] S. S. P. Parkin, Phys. Rev. Lett. **67**, 3598 (1991).

[41] A. Barthelemy and A. Fert, Phys. Rev. B **43**, 13124 (1991).

[42] B. A. Gurney, V. S. Speriosu, J. P. Nozieres, H. Lefakis, D. R. Wilhoit, and O. U. Need, Phys. Rev. Lett. **71**, 4023 (1993).

[43] M. B. Stearns, J. Magn. Magn. Mater. **5**, 167 (1977).

[44] F. J. Himpsel, K. N. Altmann, G. J. Mankey, J. E. Ortega, and D. Y. Petrovykh, J. Magn. Magn. Mater. **200**, 456 (1999).

[45] F. Manghi, V. Bellini, J. Osterwalder, T. J. Kreutz, P. Aebi, and C. Arcangeli, Phys. Rev. B **59**, R19409 (1999).

[46] C. Kittel, *Introduction to Solid State Physics*, New York, 1976).

[47] D. Y. Petrovykh, K. N. Altmann, H. Hochst, M. Laubscher, S. Maat, G. J. Mankey, and F. J. Himpsel, Applied Physics Letters **73**, 3459 (1998).

[48] S. Sahrakorpi, M. Lindroos, and A. Bansil, Phys. Rev. B **66**, 235107 (2002).

[49] D. Y. Petrovykh, K. N. Altmann, H. Höchst, M. Laubscher, S. Maat, G. J. Mankey, and F. J. Himpsel, Applied Physics Letters **73**, 3459 (1998).

[50] K. N. Altmann, N. Gilman, J. Hayoz, R. F. Willis, and F. J. Himpsel, Phys. Rev. Lett. **87**, 137201 (2001).

[51] G. Schutz, W. Wagner, W. Wilhelm, P. Kienle, R. Zeller., R. Frahm, and G. Materlik, Phys. Rev. Lett. **58**, 757 (1987).

[52] W. Kuch, J. Gilles, S. S. Kang, S. Imada, S. Suga, and J. Kirschner, Phys. Rev. B **62**, 3842 (2000).

[53] R. F. Willis, T. S. Bramfeld, and K. R. Podolak, J. Appl. Phys. **101**, 09G119 (2007).

[54] D. Schmitz, O. Rader, C. Carbone, and W. Eberhardt, Phys. Rev. B **54**, 15352 (1996).

[55] G. R. Harp, W. L. O'Brien, B. P. Tonner, and S. S. P. Parkin, J. Appl. Phys. **76**, 6462 (1994).

[56] C. Dallera, L. Braicovich, G. Ghiringhelli, N. B. Brookes, and J. B. Goedkoop, Phys. Rev. B **55**, R14729 (1997).

[57] M. M. Schwickert, G. Y. Guo, M. A. Tomaz, W. L. O'Brien, and G. R. Harp, Phys. Rev. B **58**, R4289 (1998).

[58] W. Clemens, T. Böske, C. Carbone, and W. Eberhardt, Phys. Rev. B **49**, 4003 (1994).

[59] M. D. Stiles and R. D. McMichael, Phys. Rev. B **59**, 372 (1999).

[60] T. Kai, H. Fujiwara, T. C. Schulthess, and W. H. Butler, Journal of Applied Physics **89**, 7940 (2001).

[61] J. S. Kasper and J. S. Kouvel, J. Phys. Chem. Solids **11**, 231 (1959).

[62] E. Kren, E. Nagy, I. Nagy, L. Pal, and P. Szabo, J. Phys. Chem. Solids **29**, 101 (1968).

[63] R. Thamankar, S. Bhagwat, and F. O. Schumann, J. Phys.:Condens. Matter **16**, 6029 (2004).

[64] C. Tieg, W. Kuch, S. G. Wang, and J. Kirschner, Phys. Rev. B **74**, 094420 (2006).

[65] P. Ferriani, F. Borgatti, G. Ghringhelli, A. Tagliaferri, B. D. Michelis, C. M. Bertoni, N. B. Brookes, and L. Braicovich, Phys. Rev. B **65**, 094406 (2002).

[66] J. A. Venables and C. J. Harland, Philos. Mag. **27**, 1193 (1973).

[67] A. J. Schwartz, M. Kumar, and B. L. Adams, *Electron Backscatter Diffraction in Materials Science* (Kluwer Academic/Plenum Publishers, New York, 2000).

[68] R. A. Lukaszew, Y. Sheng, C. Uher, and R. Clarke, Applied Physics Letters **76**, 724 (2000).

[69] B. G. Demczyk, V. M. Naik, A. Lukaszew, R. Naik, and G. W. Auner, Journal of Applied Physics **80**, 5035 (1996).

[70] M. Couach and A. F. Khoder, *Magnetic Susceptibility of Superconductors and other Spin Systems*, Plenum, 1992).

[71] L. L. Landau and E. M. Lifshitz, *Electrodynamics of Continuous Media* (Addison Wesley Publishing Company, Reading, 1960).

[72] E. Maxwell and M. Strongin, Phys. Rev. Lett. **10**, 212 (1963).

[73] J. R. Clem, Physica C **153-155**, 50 (1988).

[74] E. P. Wohlfarth, Physica B **86**, 852 (1977).

[75] L. Neel, Adv. Phys. **4**, 191 (1955).

[76] A. J. v. D. C. A. M. Mulder, and J. A. Mydosh, Phys. Rev. B **23**, 1384 (1981).

[77] E. M. Gray, J. Phys. F: Metal Phys. **9**, L167 (1979).

[78] C. N. Guy, J. Phys. F: Metal Phys. **7**, 1505 (1977).

[79] W. Abdul-Razzaq, J. S. Kouvel, and K. Ziq, Phys. Rev. B **35**, 1768 (1987).

[80] T. Ogawa, H. Nagasaki, and T. Sato, Phys. Rev. B **65**, 024430 (2001).

[81] Y. Oner, C. S. Lue, J. H. Ross, K. D. D. Rathnayaka, and D. G. Naugle, Journal of Applied Physics **89**, 704 (2001).

[82] D. Sherrington and S. Kirkpatrick, Phys. Rev. Lett. **35**, 1792 (1975).

[83] M. Gabay and G. Toulouse, Phys. Rev. Lett. **47**, 201 (1981).

[84] H. Naganuma, Y. Endo, R. Nakatani, Y. Kawamura, and M. Yamamoto, Science and Technology of Advanced Materials **5**, 83 (2004).

[85] E. D. Torre, L. H. Bennett, and R. E. Watson, Phys. Rev. Lett. **94**, 147210 (2005).

[86] U. Atzmony, L. J. Swartzendruber, L. H. Bennett, M. P. Dariel, D. Lashmore, M. Rubinstein, and P. Lubitz, Journal of Magnetism and Magnetic Materials **69**, 237 (1987).

[87] R. Naik, A. Poli, D. McKague, A. Lukaszew, and L. E. Wenger, Phys. Rev. B **51**, 3549 (1995).

[88] N. V. Smith, Rep. Prog. Phys. **51**, 1227 (1988).

[89] D. v. d. Marel, G. A. Sawatzky, and F. U. Hillebrecht, Phys. Rev. Lett. **53**, 206 (1984).

[90] J. Wrona, T. Stobiecki, R. Rak, M. Czapkiewicz, F. Stobiecki, L. Uba, J. Korecki, T. lzak, J. Wilgocka-lzak, and M. Rots, physica status solidi (a) **196**, 161 (2003).

[91] M. Kisielewski, Z. Kurant, A. Maziewski, M. Tekielaka, A. Wawro, A. Maneikis, and L. T. Baczewski, Journal of Magnetism and Magnetic Materials **272-276**, E861 (2004).

[92] B. R. Coles, B. V. Sarkissian, and R. H. Taylor, Phil. Mag. B **37**, 489 (1978).

[93] J. R. Childress and C. L. Chien, Phys. Rev. B **43**, 8089 (1991).

[94] C. W. Oatley, *Scanning Electron Microscope*, Cambridge, 1972).

[95] G. Goldstein, D. Newbury, P. Echlin, D. Joy, C. Fiori, and E. Lifshin, *Scanning electron microscopy and x-ray microanalysis*, New York, 1981).

VITA - Kenneth R. Podolak

The Pennsylvania State University
104 Davey Lab (Physics) Box 140
University Park, PA 16802

Email: kpod@psu.edu
Work Tel.: (814) 865-2286
Fax No.: (814) 865-3604

Education

Ph.D. Physics, The Pennsylvania State University, University Park, PA (expected 2008)
Dissertation: *Weak Ferromagnetism in Dilute Manganese-Nickel Alloys*
Advisor: Dr. Roy F. Willis

M.Ed. Master of Higher Education in Physics, The Pennsylvania State University, University Park, PA (2005)
Thesis: *Algebra-Based Physics: Pedagogical Techniques and Strategies*
Advisor: Dr. Richard Robinett

B.S. Physics (high honors), Rochester Institute of Technology, Rochester, NY (2002)

Research Experience

The Pennsylvania State University, University Park, PA (2003 – present)

- Growth of nanoscale magnetic structures via Molecular Beam Epitaxy (MBE)
- Characterization of ultrathin films with electron diffraction (LEED, RHEED) and quartz crystal microbalance (QCM)
- Use x-ray synchrotron radiation to measure angle integrated photoemission spectroscopy (PES) and magnetic circular dichroism to study magnetization
- Analysis of ferromagnetic, antiferromagnetic, and spin glass phases

Publications

- R.F. Willis, T.S. Bramfeld, **K.R. Podolak**, "Finite-size nanoscaling of the critical temperature of ferromagnets with variable range of spin interactions," Journal of Applied Physics, **101**, 09G119 (2007)
- K. R. Podolak, R.F. Willis, M. J. Wilson, & P.E. Schiffer, "Local & Non-local Magnetic Behavior of Dilute Mn-doped Nickel Alloys" (in preparation).

Teaching Experience & Awards

The Pennsylvania State University, University Park, PA

- American Association of Physics Teachers (AAPT) Outstanding Teaching Assistant (2006) & Stanley Sheperd Graduate Teaching Award (2005)
- **Teaching Assistant**, 2002 – 2008
  - Lab assistant in electronics & optics course for undergraduate majors.
  - Guest lecturer for electronics (Spring 2007) on "digital logic."
  - Taught introductory courses, including both calculus-based & algebra-based physics, that dealt with topics in mechanics, electricity & magnetism, waves & thermal, and optics & modern physics.
- **Instructor**, Physics 213 & 214: Waves, Thermal, Optics, and Modern Physics, Summer 2004 & Summer 2005
  - Responsibilities include managing teaching assistant meetings and preparing lectures, exams, and homework assignments.